Mars Climate Sounder limb profile retrieval of atmospheric temperature, pressure, and dust and water ice opacity

Armin Kleinböhl,[1] John T. Schofield,[1] David M. Kass,[1] Wedad A. Abdou,[1] Charles R. Backus,[1] Bhaswar Sen,[1] James H. Shirley,[1] W. Gregory Lawson,[2] Mark I. Richardson,[2] Fredric W. Taylor,[3] Nicholas A. Teanby,[3] and Daniel J. McCleese[1]

[1]   The Mars Climate Sounder (MCS) onboard the Mars Reconnaissance Orbiter is the latest of a series of investigations devoted to improving the understanding of current Martian climate. MCS is a nine-channel passive midinfrared and far-infrared filter radiometer designed to measure thermal emission in limb and on-planet geometries from which vertical profiles of atmospheric temperature, water vapor, dust, and condensates can be retrieved. Here we describe the algorithm that is used to retrieve atmospheric profiles from MCS limb measurements for delivery to the Planetary Data System. The algorithm is based on a modified Chahine method and uses a fast radiative transfer scheme based on the Curtis-Godson approximation. It retrieves pressure and vertical profiles of atmospheric temperature, dust opacity, and water ice opacity. Water vapor retrievals involve a different approach and will be reported separately. Pressure can be retrieved to a precision of 1–2% and is used to establish the vertical coordinate. Temperature profiles are retrieved over a range from 5–10 to 80–90 km altitude with a typical altitude resolution of 4–6 km and a precision between 0.5 and 2 K over most of this altitude range. Dust and water ice opacity profiles also achieve vertical resolutions of about 5 km and typically have precisions of 10^{-4}–10^{-5} km^{-1} at 463 cm^{-1} and 843 cm^{-1}, respectively. Examples of temperature profiles as well as dust and water ice opacity profiles from the first year of the MCS mission are presented, and atmospheric features observed during periods employing different MCS operational modes are described. An intercomparison with historical temperature measurements from the Mars Global Surveyor mission shows good agreement.

1. Introduction

[2] The Mars Climate Sounder (MCS) instrument [*McCleese et al.*, 2007] is an infrared radiometer onboard NASA's Mars Reconnaissance Orbiter (MRO) spacecraft [*Zurek and Smrekar*, 2007]. MCS is designed to take measurements of the Martian surface and atmosphere using limb, nadir, and off-nadir viewing geometries. MRO is in a polar, sun-synchronous, 0300–1500 Martian local time (MLT) orbit around Mars. This orbit provides global day and night coverage of the atmosphere, allowing diurnal and seasonal atmospheric trends to be separated. The primary goal of the MCS investigation is to characterize the present climate of Mars. It extends the climatological record established by the Thermal Emission Spectrometer (TES) on Mars Global Surveyor (MGS) [*Conrath et al.*, 2000; *M. D. Smith et al.*, 2001] by obtaining continuous measurements of atmospheric temperature, dust, water vapor and condensates. The repetitive observation of the Mars limb by MCS provides temperature profiles with an extended vertical range and improved altitude resolution compared to previous measurements, with a nearly continuous coverage. This allows global monitoring of the properties of the atmosphere with respect to atmospheric circulation, seasonal changes, and interannual climate variability. In addition the measurements give profile information on dust, water vapor, and condensates which allow the examination of the annual dust and water cycles. These measurements will address the MRO mission's objectives for the atmosphere and climate and advance our understanding of the current Mars climate. Furthermore, repeated nadir and on-planet sounding of infrared radiance and broadband solar reflec-

[1]Jet Propulsion Laboratory, California Institute of Technology, Pasadena, California, USA.
[2]Division of Geological and Planetary Sciences, California Institute of Technology, Pasadena, California, USA.
[3]Clarendon Laboratory, Atmospheric, Oceanic, and Planetary Physics, University of Oxford, Oxford, UK.

Table 1. Band Passes of the MCS Infrared Channels, Their Noise Equivalent Radiances for a 2-s Integration, and the Main Absorbers in the Martian Atmosphere at These Frequencies

Channel	Band Pass (cm^{-1})	NER $(mWm^{-2}\,sr^{-1}/cm^{-1})$	Main Absorbers
A1	595–615	0.0557	CO_2
A2	615–645	0.0399	CO_2
A3	635–665	0.0419	CO_2
A4	820–870	0.0287	H_2O ice
A5	400–500	0.0278	dust
B1	290–340	0.0453	dust
B2	220–260	0.0568	H_2O vapor, H_2O ice
B3	230–245	0.174	H_2O vapor, H_2O ice

tance will help characterize surface and subsurface thermal properties, the net polar radiative balance and the annual carbon dioxide frost budget.

[3] The Mars Climate Sounder instrument [*McCleese et al.*, 2007] is a passive nine-channel infrared radiometer. It consists of two telescopes that are designed to slew in azimuth and elevation to view the Martian atmosphere in limb, nadir, and on-planet geometries. MCS has eight midinfrared and far-infrared channels as well as a broad-band visible/near-infrared channel. This paper is focused exclusively on results from the infrared channels, which are summarized in Table 1. The channels A1, A2, and A3 cover frequencies around the 15 μm absorption band of CO_2 and are used for pressure and temperature sounding. The A4 channel centered at 12 μm covers an absorption feature of water ice, while channel A5, centered around 22 μm, gives information on dust opacity. In the far-infrared the three B channels are designed to give information about water vapor abundance and dust and water ice opacities. Each spectral channel uses a 21-element, linear detector array. When observing the atmosphere at the Mars limb, the angular separation of the individual detectors provides an altitude resolution of roughly 5 km, and the integration time for a single measurement is about 2 s. A standard measurement sequence consists of two nadir or on-planet measurements, eight consecutive limb measurements, and two space measurements for calibration. It takes about 30 s to complete. In addition measurements of a blackbody target for calibration of the infrared channels as well as measurements of a solar reflecting target for calibration of the visible channel are performed on a frequent basis [*McCleese et al.*, 2007].

[4] The MCS instrument started taking data on 24 September 2006 ($L_s = 111°$) and performed nominal limb/nadir scanning of the atmosphere until 18 January 2007. The instrument elevation actuator was not used between 9 February and 14 June 2007 because of a mechanical anomaly. During this "limb-staring" period, the detector array was pointed at the Mars limb at a constant elevation angle. Because MRO is nadir oriented, and neither the orbit nor Mars are circular, this causes systematic variations in the altitude covered by the MCS detector arrays. For example, at southern latitudes, coverage extends upward only to 55 km, whereas at northern high latitudes the lowest element of the detector array lifts off the planet by 15 km. Few space and no blackbody measurements were performed during this period, so that radiometric calibration was degraded. Fortunately, the instrument is stable enough to allow the orbital and temporal variation of calibration parameters to be interpolated across the coverage gap (J. T.

Schofield et al., manuscript in preparation (hereinafter referred to as JTS)). On 14 June 2007 the instrument resumed scanning between limb and space, with occasional slews to the internal blackbody calibration target. Since 9 October 2007 off-nadir measurements with surface incidence angles between about 60° and 70° have also been being taken again with nearly every limb sequence. At the time of writing MCS has completed more than 1 Mars year of observations.

[5] This paper deals with the retrieval process used to obtain pressure information, temperature profiles, and profiles of dust and water ice opacity from limb radiance measurements to generate the current Level 2 data product (vertical profiles of geophysical parameters) of the MCS investigation delivered to the Planetary Data System (PDS). We describe the radiative transfer and the simplifications that have been implemented to accommodate a timely retrieval even with the 30 s measurement repeat cycle. We introduce the retrieval algorithm, which is based on the method by *Chahine* [1970], and describe how it is applied to MCS data to retrieve vertical profiles of the desired quantities. Examples of retrievals are given and their vertical coverage and resolution is discussed. We also give a description of the Level 2 data set that has been provided to the PDS. The validity of the retrieval algorithm is examined by analyzing simulated radiances. Then we present results of the global temperature, dust, and water ice retrievals of the first Mars year of MCS measurements and investigate latitudinal differences and seasonal changes. Finally we compare retrieved MCS profiles with the results of the radio science and TES investigations for earlier Mars years from the MGS mission and summarize our plans for further improvements to the retrieval algorithm.

2. Radiative Transfer

2.1. Spectroscopy

2.1.1. Gases

2.1.1.1. CO_2

[6] In the Martian atmosphere gaseous absorption in the frequency range covered by MCS is dominated by the vibrational and rotational bands of CO_2 and H_2O. Other gases have negligible contributions at the concentrations found in the Martian atmosphere. CO_2 is the dominant gaseous absorber in the channels A1 to A4. In channel A5 water vapor tends absorb more strongly than CO_2 if significant amounts are present in the Martian atmosphere. For the B channels only water vapor absorption is important.

[7] Gaseous absorption is described by the absorption coefficient $k(\nu)$. A transition between discrete vibration-rotation states in a gas results in a spectral line in the absorption coefficient, which can be written as

$$k(\nu) = U \cdot S(T) \cdot f(\nu). \qquad (1)$$

[8] Here U is the absorber amount, $S(T)$ is the line intensity as a function of temperature, and $f(\nu)$ is the line shape function versus frequency, normalized such that

$$\int f(\nu)d\nu = 1. \qquad (2)$$

[9] The spectroscopic parameters used for the gaseous radiative transfer are based on the 2004 HITRAN line list [*Rothman et al.*, 2005]. Essential parameters for CO_2, given by the HITRAN line list, are line position, line intensity, lower state energy, and self-broadened half width. Temperature dependencies for pressure broadening are only given for broadening in air, not for broadening in CO_2. To estimate a self-broadened half width from the given air-broadened half width we rely on calculations by *Yamamoto et al.* [1969]. They provide calculated pressure-broadened half widths of CO_2 for broadening by both N_2 and CO_2 at three different temperatures ranging from 180 to 300 K, as a function of the rotational quantum number of the initial state of the transition. The temperature dependence of line broadening is represented by fitting these calculations to the expression

$$\gamma(T) = \gamma(T_{ref}) \cdot \left(\frac{T_{ref}}{T}\right)^n \qquad (3)$$

for broadening by both CO_2 and N_2, where T_{ref} is a reference temperature and n is the exponent of the temperature dependence. The temperature exponent for broadening in CO_2 used in the radiative transfer calculation is then scaled from HITRAN air broadening as

$$n_{CO_2} = n_{air,HITRAN} \cdot \frac{n_{CO_2,Yamamoto}}{n_{N_2,Yamamoto}} \qquad (4)$$

according to the rotational quantum number of the initial state for each line.

[10] Line shapes of absorption lines are approximated by the Voigt function. This is a convolution of a Gaussian which represents the Doppler broadening of a line, and a Lorentz function, which represents the pressure broadening of a line. However, for self-broadened CO_2 lines the absorption beyond a few wave numbers off the line center is lower than predicted by a Lorentz function [*Burch et al.*, 1969]. The line shape f for such a line can be described by the Lorentz function f_L multiplied by a factor χ which depends on the distance from the line center:

$$f = f_L \cdot \chi(\nu - \nu_0). \qquad (5)$$

[11] To obtain a functional value for χ the data for self-broadened CO_2 presented by *Burch et al.* [1969, Figure 14] has been fitted between 6 and 300 cm^{-1} (P. Irwin, personal communication, 2007). These data were measured in the 2400 cm^{-1} region which is the lowest frequency where data are available. Using a polynomial to ensure a smooth transition between 3 and 6 cm^{-1} we obtain

$$\chi = \begin{cases} 1; |\nu - \nu_0| \leq 3\mathrm{cm}^{-1} \\ \begin{aligned} &-1.40253 \\ &+1.92162|\nu - \nu_0| \\ &-4.79585 \cdot 10^{-1}|\nu - \nu_0|^2 \\ &+3.53706 \cdot 10^{-2}|\nu - \nu_0|^3; 3\mathrm{cm}^{-1} < |\nu - \nu_0| \leq 6\mathrm{cm}^{-1} \end{aligned} \\ 10^{-0.233-1.087\cdot10^{-2}|\nu-\nu_0|}; 6\mathrm{cm}^{-1} < |\nu - \nu_0| \leq 46\mathrm{cm}^{-1} \\ 10^{-0.133-1.3\cdot10^{-2}|\nu-\nu_0|}; 46\mathrm{cm}^{-1} < |\nu - \nu_0| \leq 136\mathrm{cm}^{-1} \\ 10^{-0.7-8.8\cdot10^{-3}|\nu-\nu_0|}; |\nu - \nu_0| > 136\mathrm{cm}^{-1}. \end{cases} \qquad (6)$$

[12] The CO_2 volume mixing ratio is assumed to be at a constant value of 0.9532, as measured by *Owen et al.* [1977] at the surface of Mars using the mass spectrometer on the Viking lander. Isotopic ratios are assumed to be the same as in the HITRAN database.

2.1.1.2. H₂O

[13] The HITRAN line list provides line position, line intensity, and lower state energy for a tremendous number of water vapor transitions [*Rothman et al.*, 2005]. However, broadening parameters are given only for broadening in air and water vapor itself, not in CO_2. *Brown et al.* [2007] present measurements of CO_2-broadened half width for water vapor lines in the ν_2 fundamental band. The measurements are compared with calculations based on the complex Robert-Bonamy theory. Generally good agreement between measurements and calculations gave rise to predictions of CO_2-broadened half widths and their temperature dependencies for the pure rotational band between 200 and 900 cm-1, which are also reported by *Brown et al.* [2007]. These are used for the MCS radiative transfer calculations. For water vapor lines a Voigt line shape is used. We use the isotopic fractionation of standard mean ocean water for water molecules with heavy oxygen isotopes. For HDO a D/H ratio enhanced by a factor of 5.5 is assumed [*Krasnopolsky et al.*, 1997].

2.1.2. Dust/Condensates

2.1.2.1. Dust

[14] We use Mie theory to calculate dust extinction efficiencies for all channels. The calculations are based on the refractive indices of Martian dust obtained from analyses of measurements from TES on MGS and MiniTES on the Mars Exploration Rovers [*Wolff et al.*, 2006]. Because no data from these sources is available in the frequency region of the main CO_2 absorption ($560-780$ cm^{-1}) we use the refractive indices of basalt (J. Bandfield and T. Glotch, personal communication, 2007), scaled to match smoothly to the Martian dust data, to bridge the gap. In the far infrared (below ~ 380 cm^{-1}) we use data based on the work by *Hansen* [2003]. Figure 1 shows the refractive indices versus frequency.

[15] The Mie calculations assume particles of spherical symmetry with radii on the basis of a modified gamma distribution:
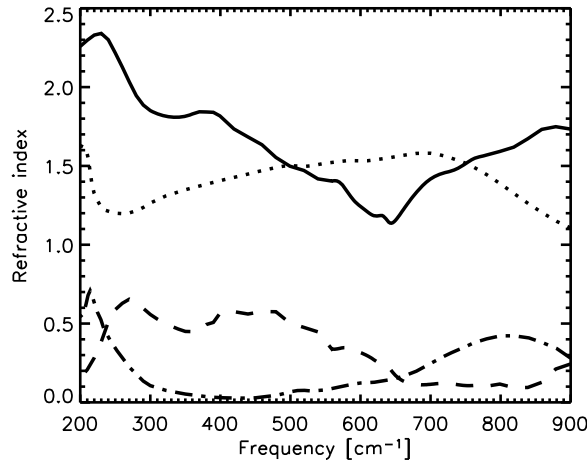
$$n(r) \sim r^a e^{-br^c}. \qquad (7)$$

[16] Here n is the number of particles with radius r, and a, b, and c are the parameters describing the distribution. For the dust distribution we adapt the parameters derived from the recent study of *Wolff et al.* [2006], which are $a = 2$, $b = 8.15$, and $c = 0.52$. With the definition of

$$G = \int \pi r^2 n(r) dr \qquad (8)$$

the effective radius for the particle distribution

$$r_{eff} = \frac{1}{G} \int r \pi r^2 n(r) dr \qquad (9)$$

Figure 1. Refractive indices used in Mie calculations: real index for dust (solid), imaginary index for dust (dashed), real index for water ice (dotted), and imaginary index for water ice (dash-dotted).

is calculated to be r_{eff} = 1.5 μm, as quoted in their paper. The dimensionless effective variance of the distribution, defined as

$$v_{eff} = \frac{1}{Gr_{eff}^2} \int (r - r_{eff})^2 \pi r^2 n(r) dr, \qquad (10)$$

is v_{eff} = 0.4.

[17] From the Mie calculations we obtain extinction efficiencies over the frequency range covered by MCS. These extinction efficiencies are averaged over the frequency bands of the different MCS channels. Table 2 gives the band averaged extinction efficiencies and the center frequencies of each channel. Dust opacities are reported for a frequency of 463 cm^{-1}, corresponding to the center frequency of channel A5. Assuming the dust model outlined above, opacities at visible wavelengths ($\sim$600 nm) would be higher than the retrieved infrared opacities by about a factor of 4.4. Scattering has not yet been included in the MCS retrieval scheme. Instead dust is considered to be entirely absorbing with an absorption efficiency that equals Q_{ext}.

2.1.2.2. Water Ice

[18] Water ice is the most widespread condensate in the Martian atmosphere. We use the same approach based on Mie theory to calculate extinction efficiencies for water ice in all spectral channels. The refractive indices used for these calculations are the ones reported by *Warren* [1984]. They are shown in Figure 1 over the MCS frequency range.

[19] As for the dust, we use a modified gamma distribution to represent the sizes of the ice particles in the Mie calculations. Analyses of the size distribution of water ice particles based on MGS TES data give r_{eff} = 1−2 μm for ice hazes between 20 and 40 km altitude and r_{eff} = 3−4 μm in the aphelion cloud belt [*Wolff and Clancy*, 2003; *Clancy et al.*, 2003]. At higher altitudes lower particle sizes have been reported [*Montmessin et al.*, 2006]. Recent work by *Fedorova et al.* [2009] suggests particle sizes with effective

radii around 0.5−1.5 μm between about 20−60 km altitude. We chose the simple parameters a = 2, b = 2, and c = 1.5 for equation (7). This gives an effective radius of r_{eff} = 1.36μm, which seems to be a good compromise for the reported size ranges and gives good results over a large fraction of the MCS data. The effective variance of v_{eff} = 0.14 is also within the range suggested by these observations. The band averaged extinction efficiencies for the MCS channels obtained by the Mie calculations are given in Table 2. Again scattering is not considered and water ice is assumed to be entirely absorptive. Water ice opacities are reported with respect to the center frequency of the A4 channel which is 843 cm^{-1}. With the assumed ice model, opacities at visible wavelengths ($\sim$600 nm) would be higher by about a factor of 3.3 compared to the infrared opacities.

2.1.2.3. Effect of Aerosol Scattering

[20] In the present work, the scattering of radiation into the limb path by aerosols is neglected. MCS retrievals containing a single scattering approximation are now being tested, and will be reported in a future paper. This paper describes the analysis behind the data currently released to the PDS.

[21] Aerosol radiative transfer in the nonscattering case is represented by setting Q_{abs}: = Q_{ext}. This approximation represents the transmissive part of the radiative transfer equation correctly, and is equivalent to assuming that the internal radiation field is isotropic and equal in intensity to the emissive source function at a given point in the atmospheric limb path. As the internal radiation field is dominated by surface emission under most conditions, the approximation overestimates the effect of scattering at night and underestimates it during the day by an amount that depends on the single scattering albedo of the aerosol, the temperature contrast between the surface and the atmosphere, and wavelength. The largest effects are likely to be seen on the dayside in the shortest wavelength channels, where the contrast between surface and atmospheric emission is greatest.

[22] Errors in limb radiance resulting from this approximation have been studied with a multiple scattering code that uses a plane parallel approximation to the internal radiation field [*Irwin*, 2007]. Similar tests have also been performed using 3-D Monte Carlo models [*Whitney et al.*, 1999; *Wolff et al.*, 2006; *Clancy et al.*, 2007]. In the latter case, a TES equatorial temperature profile with a surface temperature of 270 K was used. For uniformly mixed dust (r_{eff} = 1.5μm, v_{eff} = 0.4) the approximation underestimated limb radiance by up to 10% in A5 limb profiles for the lowest column opacities and highest altitudes. The dust retrieval might therefore be expected to overestimate dust optical depth by 10% under similar conditions. Calculations of A4 limb radiance profiles for the same atmospheric

Table 2. Center Frequencies and Extinction Efficiencies for Dust and Water Ice for the MCS A Channels[a]

Channel	A1	A2	A3	A4	A5
Center frequency	606.916	631.017	648.703	842.724	463.436
Q_{ext} (Dust)	0.4483	0.3783	0.3006	0.5979	0.5473
Q_{ext} (H$_2$O ice)	0.1851	0.2138	0.2455	0.7467	0.0457

[a]Center frequencies are in cm^{-1}.

model containing uniformly mixed water ice ($r_{eff} = 2.0\,\mu$m, $v_{eff} = 0.1$) limited to $25-50$ km, revealed underestimates of 30% in limb radiance for lower ice abundances at the higher levels, suggesting that the retrieval would overestimate ice optical depth by 30%. These are representative estimates of the worst case errors expected for equatorial dayside conditions.

[23] Several observations have suggested the presence of CO_2 ice in the Martian atmosphere, either close to the ground in the winter polar atmosphere [*Zuber et al.*, 1998], or as hazes at high altitudes [*Montmessin et al.*, 2007]. As CO_2 ice is highly scattering at infrared frequencies [*Hansen*, 1997], we do not attempt a retrieval of CO_2 ice at this stage.

2.2. Curtis-Godson Approximation

2.2.1. Theoretical Basis

[24] The forward calculation is based on the radiative transfer equation which can be written as

$$R = \int_\nu F(\nu) \int_z B(\nu, T(z)) K(\nu, z)\, dz\, d\nu, \qquad (11)$$

where R is the radiance seen in a certain channel at space along the view vector and $F(\nu)$ is the frequency response of the channel. B is the Planck function. $K(\nu, z)$ is the vertical response or weighting function at frequency ν, defined as

$$K(\nu, z) = \frac{d\Upsilon(\nu, z)}{dz}, \qquad (12)$$

where $\Upsilon(\nu, z)$ is the transmission from altitude z to space.

[25] In numerical radiative transfer calculations the atmosphere is represented as layers, which we assume are spherically homogeneous. We illustrate this for a path that intersects the surface, assumed to have an emissivity of one. Then the radiative transfer equation will be

$$R = \int_\nu \left[F(\nu) \left(\epsilon B(\nu, T_{surf}) \Upsilon_{surf}(\nu) + \sum_i B(\nu, T_{e,i}) K_i(\nu) \right) \right] d\nu, \qquad (13)$$

where the first term is the surface contribution (ϵ being the surface emissivity) and the second term is a sum over the layers between the surface and the spacecraft ($T_{e,i}$ being the temperature of the emitting layer). In case of a limb view that does not intersect the surface the second term runs over the layers from the tangent point to the spacecraft, and the first term is replaced by a summation from the tangent point to space in the opposite direction to describe the atmospheric radiation beyond the tangent point. The weighting functions are then given by

$$K_i(\nu) = \Upsilon_{i+1}(\nu) - \Upsilon_i(\nu), \qquad (14)$$

where the $\Upsilon_i(\nu)$ are the transmissions from layer i to space at frequency ν.

[26] In line-by-line radiative transfer models these transmissions can be calculated on a frequency grid appropriate for the application as a product from the considered layer i to the top layer in the atmosphere n,

$$\Upsilon_i(\nu) = \prod_{j=i}^{n} e^{-k_j(\nu) U_j}, \qquad (15)$$

where U_j is absorber amount and $k_j(\nu)$, the monochromatic absorption coefficient of layer j, is a function of mean layer pressure P and temperature T. U, P, and T are determined by viewing geometry, atmospheric temperature and absorber mixing ratio profiles. The integral over the channel's spectral bandpass in equation (13) is performed after the transmission calculations.

[27] As a full line-by-line calculation is impractical for the operational retrieval we use approximations to increase the speed of the computations. We write a band-averaged radiative transfer equation as

$$R = \epsilon B(\nu_0, T_{surf}) \langle \Upsilon_{surf} \rangle + \sum_i B(\nu_0, T_{e,i}) \langle K_i \rangle, \qquad (16)$$

where the Planck function is now calculated with respect to the central frequency of a channel ν_0 and the temperature of the emitting layer $T_{e,i}$, and transmissions and weighting functions are defined to be band averaged, denoted by angle brackets. The weighting functions are now simply defined as

$$\langle K_i \rangle = \langle \Upsilon_{i+1} \rangle - \langle \Upsilon_i \rangle. \qquad (17)$$

[28] We obtain these band-averaged transmissions by applying a modified Curtis-Godson approximation. The Curtis-Godson approximation [*Curtis*, 1952; *Godson*, 1953] seeks to simplify equation (15) by defining a single homogeneous path that approximates closely to the line-of-sight atmospheric path as far as its band-averaged transmission to space is concerned. We use a modified version of this approximation in which the path parameters are given by

$$\overline{U} = \sum_i U_i, \qquad (18)$$

$$\overline{P} = \frac{\sum_i U_i P_i}{\sum_i U_i}, \qquad (19)$$

$$\overline{T} = \frac{\sum_i U_i P_i T_i}{\sum_i U_i P_i}. \qquad (20)$$

[29] Here U_i, P_i, and T_i are the amount, pressure and temperature for layer i. The summation runs along the optical path. Note that the path-averaged temperature in this approach also depends on pressure, not only on temperature and amount. This tends to give better results in the Martian atmosphere than the commonly used formulation, in which path-averaged temperature only depends on temperature and amount. The success of the modified approximation derives from the enormous CO_2 path lengths encountered in the Martian atmosphere. Under these conditions, radiation to space at most levels is dominated by far-Lorentz line wings, where transmissions are proportional to PU, and line centers are black. In channels centered on the 15 μm band, line centers only contribute significantly to radiation to space above 60 km.

2.2.2. Transmission Tables

[30] The Curtis-Godson approximation allows transmission to be interpolated rapidly from precalculated, band-

averaged transmission tables for a single homogeneous path covering the range of $\overline{U}$, $\overline{P}$, and $\overline{T}$ expected in the Martian atmosphere. In the retrieval, this calculation is simplified by treating different atmospheric absorbers independently, such that

$$\Upsilon_i = \Upsilon_{i,\mathrm{CO_2}} \cdot \Upsilon_{i,\mathrm{H_2O}} \cdot \Upsilon_{i,\mathrm{dust}} \cdot \Upsilon_{i,\mathrm{ice}}; \qquad (21)$$

that is band-averaged transmission is assumed to be the simple product of band-averaged transmissions for CO_2, H_2O, dust, and ice. This is a reasonable assumption if one gaseous absorber is dominant and dust and ice are treated as gray absorbers with no wavelength dependence of optical depth within the channel bandpass (i.e., $\Upsilon_{i,\mathrm{dust}} = e^{-\tau_d}$, where τ_d is dust optical depth above level i integrated along the view vector).

[31] In order to be consistent with the radiance calculation of equation (16), the band-averaged transmission of a homogeneous path for a channel is defined by

$$\Upsilon = \frac{\int B(\nu, T)\Upsilon(\nu)F(\nu)d\nu}{B(\nu_0, T_e)\int F(\nu)d\nu}, \qquad (22)$$

where $F(\nu)$ is the frequency response of the channel. Band-averaged transmissions are calculated using a line-by-line program [McCleese et al., 1992], which calculates all lines with no approximations, using a look-up table for the Voigt line shape. It performs the summation of equation (22) over a frequency grid of 0.0005 cm^{-1} in the A channels, which is fine enough to sample all spectral features adequately. Going to a frequency grid of 0.00025 cm^{-1} produces changes of less than 0.2% at altitudes where the individual channels A1, A2, and A3 are used.

[32] Transmission tables are calculated for each channel and gaseous absorber where significant. They are given in the dimensions of temperature, pressure, amount, and temperature of the emitting layer, which is not necessarily equal to the Curtis-Godson path temperature given by equation (20). Transmissions are calculated at 10 K temperature intervals and at geometrical intervals of $e^{1/2}$ in pressure and amount as defined in the following equations:

$$T = 110 + 10i \text{ [K]}; \ 0 \le i \le 22, \qquad (23)$$

$$P = 0.01e^{-j/2} \text{ [bar]}; \ 0 \le j \le 33, \qquad (24)$$

$$U_{\mathrm{CO_2}} = 10\frac{e^{-j/2}}{e^{-k/2}} \ [\mathrm{g \cdot cm^{-2}}]; \ 0 \le k \le 13, \qquad (25)$$

$$U_{\mathrm{H_2O}} = 6.25 \cdot 10^{-7}\frac{e^{-j/2}}{e^{-k/2}}[\mathrm{g \cdot cm^{-2}}]; 0 \le k \le 33, \qquad (26)$$

$$T_e = T + 10l \text{ [K]}; \ -2 \le l \le 2. \qquad (27)$$

[33] The temperature grid range of 110 to 330 K covers all homogeneous path temperatures expected in the Martian atmosphere. The grid for the temperature of the emitting layer has 5 steps that are coupled to the temperature grid.

The pressure grid ranges from 0.01 bar to 6.8 10^{-10} bar, which is adequate for the homogeneous path pressures encountered below 120 km. The amount grids cover the ranges $6.8 \cdot 10^{-7}$ to $4.0 \cdot 10^3$ g · cm^{-2} for CO_2 and $4.2 \cdot 10^{-14}$ to 9.2 g · cm^{-2} for H_2O. They are scaled by pressure to reduce their sizes.

[34] For the radiative transfer calculations, homogeneous paths for temperature, pressure and amount are determined, and the corresponding transmissions are interpolated from the transmission tables. For CO_2 transmissions in the channels A1, A2, and A3 a four-point third-order polynomial interpolation is used in temperature, ln(pressure), ln(amount) with a linear interpolation in emitting temperature to ensure the calculation of sufficiently smooth weighting functions. For CO_2 transmissions in the channels A4 and A5 as well as for H_2O transmissions a quadrilinear interpolation is used for all dimensions.

2.2.3. Comparison to Line-by-Line Calculations
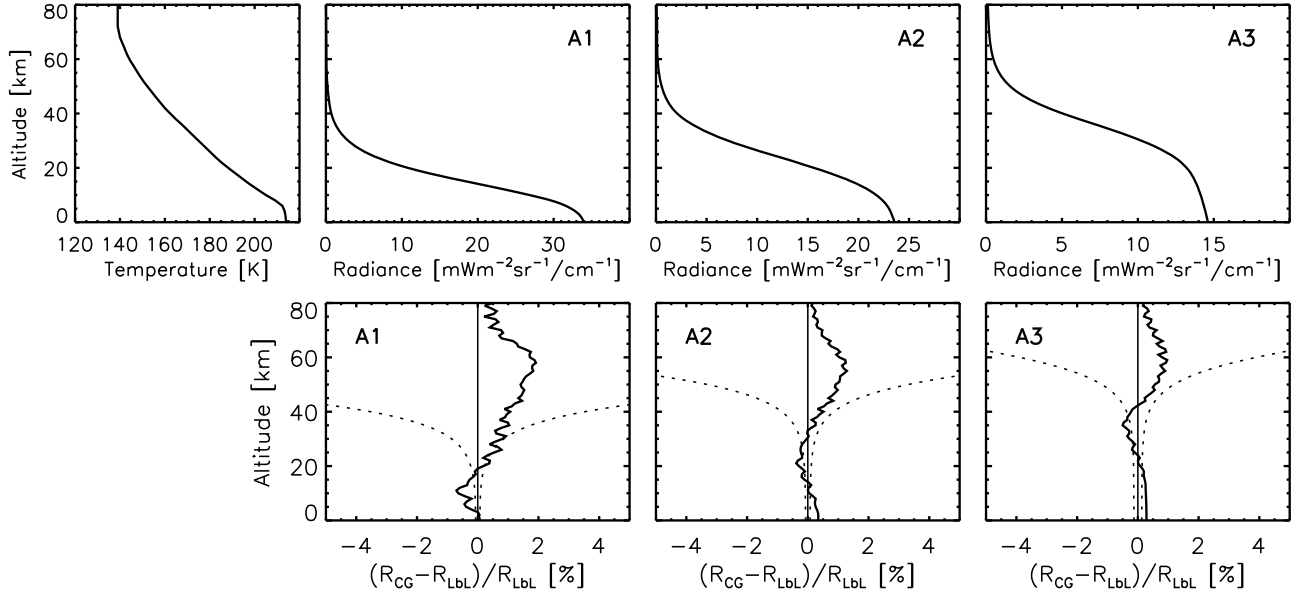
[35] To test the Curtis-Godson approximation, radiances are calculated for limb views at different tangent altitudes for different atmospheric profiles by the line-by-line radiative transfer program, and compared to the output of the radiative transfer scheme based on the Curtis-Godson approximation with transmission tables as applied in the retrieval program. Figures 2 and 3 show the results of these comparisons for a northern midlatitude summer atmosphere and a southern polar winter atmosphere, respectively.

[36] Figure 2 shows the comparison of the Curtis-Godson approximation with a line-by-line calculation in a northern midlatitude summer atmosphere for the MCS channels with significant CO_2 absorption. The temperature profile as well as the calculated radiance profiles are given in Figure 2 (top), while the percentage differences are given in Figure 2 (bottom), with the error due to the noise equivalent radiance of an average of five individual measurements shown for comparison. For the channels A1 and A2 one can see that the differences between the Curtis-Godson approximation and the line-by-line calculation are well below 1% in the altitude range where noise does not have a significant influence on the signal. For channel A3 the difference is below 0.5% in this altitude range, and still below 1% above.

[37] A comparison for a temperature profile representing a southern polar winter atmosphere is presented in Figure 3. This is a challenging atmosphere for a Curtis-Godson approximation because of the temperature inversion in the middle atmosphere, which exhibits steep temperature gradients. In channel A1 the differences between the Curtis-Godson approximation and the line-by-line calculation are less than 1% below 15 km, and rise to just above 2% between 20 and 30 km. The differences in the A2 channel, which is more likely to be used for retrievals at altitudes above 20 km, are smaller and stay below 1.5% throughout the altitude range where the signal is significantly above the noise. For channel A3 the difference is below 1% in this altitude range, and below 1.5% above.

2.3. Non-LTE Parameterization

[38] The strongest CO_2 vibrational bands are in local thermal equilibrium (LTE) in the lower and middle Martian atmosphere. However, above $\sim$80 km local thermal equilibrium starts to break down even for the CO_2 fundamental band at 15 μm [Lopez-Valverde and Lopez-Puertas, 1994a],
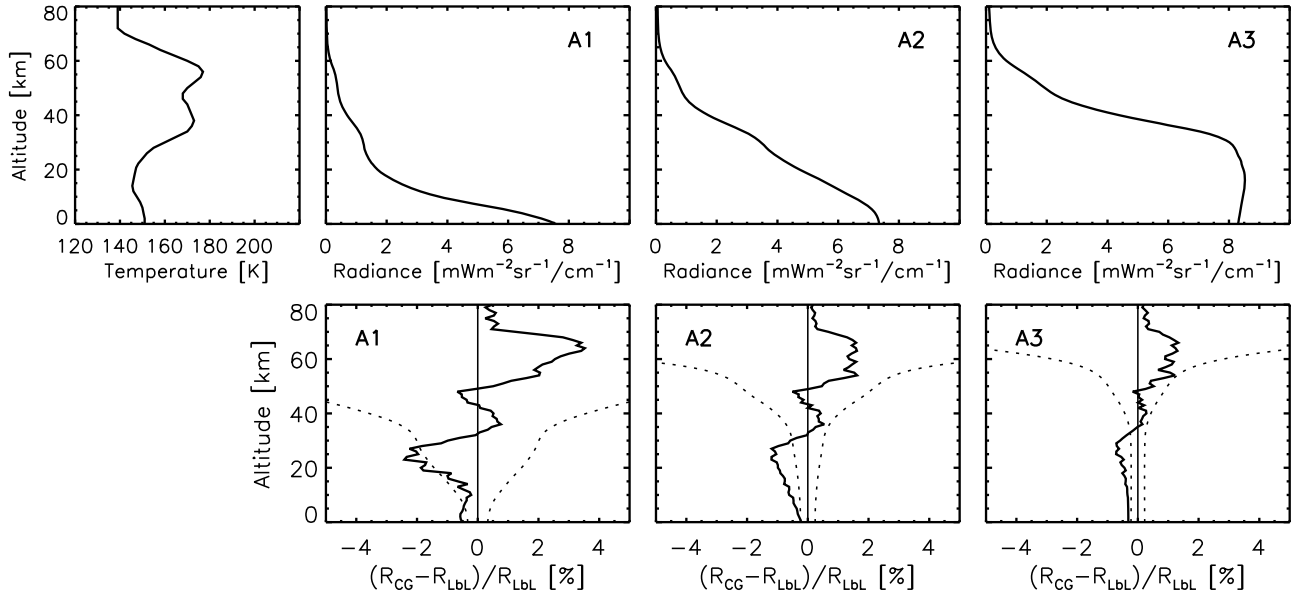
Figure 2. (top) Northern midlatitude summer temperature profile and radiances calculated from it for the MCS channels A1, A2, and A3. (bottom) Percentage differences between radiances calculated using the Curtis-Godson approximation (R_{CG}) and a line-by-line calculation (R_{LbL}) for the MCS channels A1, A2, and A3 (solid lines). The dashed lines give the noise equivalent radiance difference of an average of five individual radiance measurements.
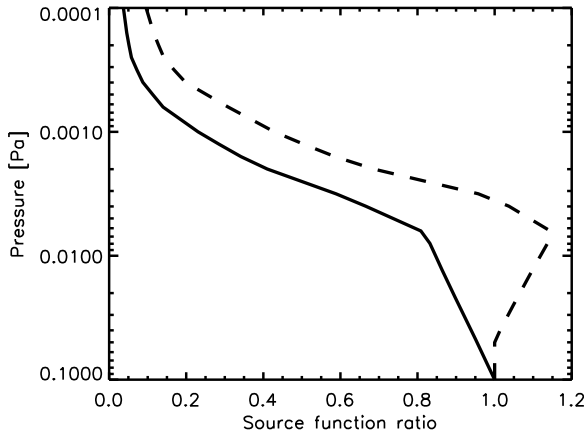
which is used for temperature retrieval at high altitudes by MCS. Therefore it was decided to include a simple parameterization to take non-LTE effects for this band into account. We use the vibrational and kinetic temperatures given by *Lopez-Valverde and Lopez-Puertas* [1994a] for nighttime conditions and by *Lopez-Valverde and Lopez-Puertas* [1994b] for daytime conditions to create source function ratios that are dependent on pressure. They are shown in Figure 4. A source function ratio is the ratio of an emission divided by the emission given by the Planck function. The source function ratio is unity in case of LTE. If the vibrational temperature is lower than the kinetic temperature the source function ratio is lower than one. In daytime conditions around 0.01 Pa the source function ratio is actually greater than one, mostly because of deactivation of higher CO_2 overtone levels pumped by solar absorption in the near infrared [*Lopez-Valverde and Lopez-Puertas*, 1994b].

[39] We tabulate the source function ratios for day and night between 0.1 and 0.0001 Pa (roughly 75 to 135 km)

Figure 3. As in Figure 2 but for southern polar winter temperature profile.

Figure 4. Non-LTE source functions for nighttime (solid) and daytime ($sza = 0°$, dashed).

such that we can calculate an appropriate source function ratio (src) depending on solar zenith angle (sza) for the pressure at each level in the radiative transfer scheme using

$$src = \begin{cases} src_{night}; & sza \geq 90°, \\ src_{night} \\ + (src_{day} - src_{night}) \cdot \cos(sza); & 0° < sza < 90°. \end{cases} \quad (28)$$

[40] This source function ratio is applied in the calculation of the radiance for the A3 channel, which is dominated by the emission of the 15 μm band. The resulting corrections tend to be small at the altitudes the top detector of the MCS array is typically pointing to. They correspond to temperature differences in the order of $2-4$ K at $80-90$ km altitude.

3. Retrieval

3.1. Theoretical Basis

[41] The retrieval algorithm is based on a method developed by *Chahine* [1970, 1972] as a general relaxation method for the retrieval of atmospheric temperature and constituents from remote sounding measurements. It uses an iterative approach to invert the radiative transfer equation and determine the atmospheric state (temperature and/or absorber amount) implied by the measured radiances. This inversion is nonunique as equation (11) is generally not amenable to a closed form inversion. We want to express the dependence between atmospheric state and radiances simplified as

$$\mathbf{R} = \mathbf{A}\mathbf{f}, \quad (29)$$

where $\mathbf{f}$ is the atmospheric state and $\mathbf{A}$ is the forward operator used to calculate radiances $\mathbf{R}$ from $\mathbf{f}$. Typically $\mathbf{R}$ and $\mathbf{f}$ are vectors because there will be several radiance measurements and many values in $\mathbf{f}$ (e.g., temperature on altitude levels).

[42] The approach in Chahine's method is to perform a radiance calculation with a guess of $\mathbf{f}$ and derive scale factors $\mathbf{s}$ to perturb $\mathbf{f}$ by comparing measured with calculated radiances. The idea is that the scale factors should always move $\mathbf{f}$ into the direction toward the solution. The

simplest example of a scale factor would be a quotient of the measured and calculated radiances

$$\mathbf{s} = \frac{\mathbf{R_m}}{\mathbf{R_c}}. \quad (30)$$

[43] This would give the solution for an absorber amount in an optically thin isothermal atmosphere where radiance is essentially proportional to absorber amount. For other cases more sophisticated definitions of $\mathbf{s}$ may be more suitable. One approach is to reduce the step size in the case where the atmosphere is not optically thin. Another approach is to use brightness temperature ratios instead of radiance ratios to retrieve temperature. The approaches used in the MCS retrieval will be described in section 3.2.

[44] The original formulation of Chahine's method assumed an equal number i of radiance measurements and elements of $\mathbf{f}$, where the individual f_i were to be defined on the levels of maximum response to the measurement of R_i [*Chahine*, 1970]. In the modified method used here it is desirable to have a common basis for the elements of $\mathbf{f}$ (e.g., a fixed altitude grid). Assuming $\mathbf{f}$ has j elements, the information of the i measurements now has to be appropriately distributed over the j elements. This is achieved with the weighting functions as they describe the sensitivity of a measurement i to the individual f_j. Hence we define a vector of scale factors $\mathbf{s}'$ with j elements

$$s_j' = \left(\sum_i s_i \cdot K_{j,i} \right) \Big/ \sum_i K_{j,i}. \quad (31)$$

[45] Using this in an iterative procedure with n as the iteration number we can write

$$f_j^{(n+1)} = s_j'^{(n)} f_j^{(n)}. \quad (32)$$
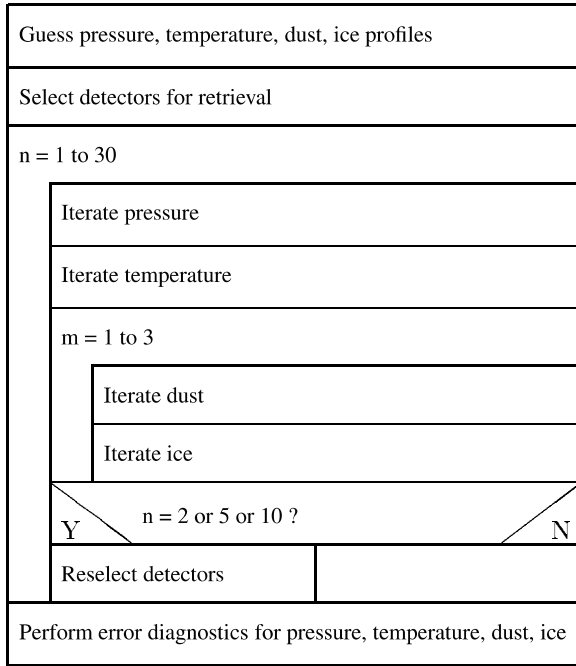
[46] The algorithm to perform the retrieval of a given quantity using Chahine's method would then look like this: (1) guess a starting value for the retrieved quantity $\mathbf{f}$ and perform a forward calculation to obtain radiances, (2) perturb quantity to be retrieved using scale factors $\mathbf{s}'$, (3) perform a forward calculation and compare calculated with measured radiances, and (4) continue with the second step until a convergence criterion or a maximum number of iterations is reached.

[47] The retrieval of more than one quantity may require a more sophisticated iteration sequence. If the different quantities interact they will have to be retrieved in a combined iteration loop and care has to be taken concerning the speed with which convergence is reached for the different quantities.

3.2. Implementation

3.2.1. Geometry

[48] The retrieval is performed on a regular altitude grid with 1 km spacing. Analyses of the field-of-view (FOV) wings of the MCS detectors (JTS) suggest that a range from 40 km below the surface to 120 km above the surface is appropriate. The retrieval assumes local spherical symmetry and horizontal homogeneity within an altitude layer. A limb

Guess pressure, temperature, dust, ice profiles
Select detectors for retrieval
n = 1 to 30
Iterate pressure
Iterate temperature
m = 1 to 3
Iterate dust
Iterate ice
Y   n = 2 or 5 or 10 ?   N
Reselect detectors
Perform error diagnostics for pressure, temperature, dust, ice

Figure 5. Top level structure of the MCS retrieval algorithm.

retrieval typically uses an average of five individual measurements. In the nominal scanning sequence eight 2-s limb observations are acquired bracketed by on-planet observations or space calibrations. It was recognized that the first three of these limb measurements tend to contain thermal transients from the preceding, warmer, on-planet observations so the use of the last five measurements in a sequence of eight ensures that the analyzed measurements are free of transients. The FOV of each individual detector in each individual measurement is projected on the altitude grid using the geometry information from the spacecraft. Then the projected FOVs are averaged over the five measurements to yield a combined FOV for each detector which is used in the retrieval.

[49] We use the topography derived from the Mars Orbiter Laser Altimeter (MOLA) at a resolution of 1/16 degree per pixel [*D. E. Smith et al.*, 2001] to define the surface. From this information a horizon is calculated across the FOV of the MCS detector array. The surface of the altitude grid is determined as the horizon below the boresight of the detector array. Note that because of the uncertainty in the spacecraft geometry this surface is defined only to an accuracy of about 1 km. In addition to the surface in the retrieval grid the retrieval program stores surface information at the horizontal positions of the individual MCS channels. This is relevant for the selection of detectors for retrieval in case there is a significant slope in the horizon across the MCS detector array, either because of the spacecraft orientation or the local topography.

3.2.2. Algorithm Structure

[50] A top level diagram of the structure of the algorithm is given in Figure 5. We start with a first guess of pressure, temperature, dust, and water ice and select appropriate detectors for retrieval. We perform a fixed number of iterations (loop *n* in Figure 5) which is currently set to 30.

As the changes in the dust and ice profiles may cover several orders of magnitude, and hence tend to be significantly larger than for pressure and temperature, it turned out to be advantageous to iterate them more often than the pressure and temperature profiles. This is achieved by having an inner loop (loop *m* in Figure 5) that iterates dust and ice 3 times for every iteration in pressure and temperature. Three times during the retrieval the selection of detectors is reevaluated to accommodate the changes in the profiles during the retrieval process. At the end of the retrieval, error diagnostics are performed for all retrieved quantities.

3.2.3. First Guess

[51] As the Chahine method is an iterative retrieval method a first guess has to be selected for each of the quantities retrieved. Note that although a first guess close to the solution helps the convergence of the retrieval, sensitivity studies showed that it is not essential for the success of a retrieval (see section 4.3 for an example).

[52] For the atmospheric temperature profile we use climatological information based on the Mars Weather Research and Forecasting (WRF) general circulation model [*Richardson et al.*, 2007]. The model was run over 3 Mars years with a prescribed dust forcing scheme appropriate for a year without a global dust storm, and the last year was analyzed. The climatology was built by averaging the model output zonally in 10° latitude bins and 30° intervals of L_s at local times of 3.5 h and 15.5 h. To calculate a temperature first guess the climatology is interpolated in latitude, L_s, and local time, and the resulting temperature profile is smoothed with a square 5 km wide function to take out features that cannot be resolved by the MCS measurements. A similar climatology for surface temperature is derived from the same model run, and a surface temperature first guess is also obtained by interpolation in latitude, L_s, and local time.
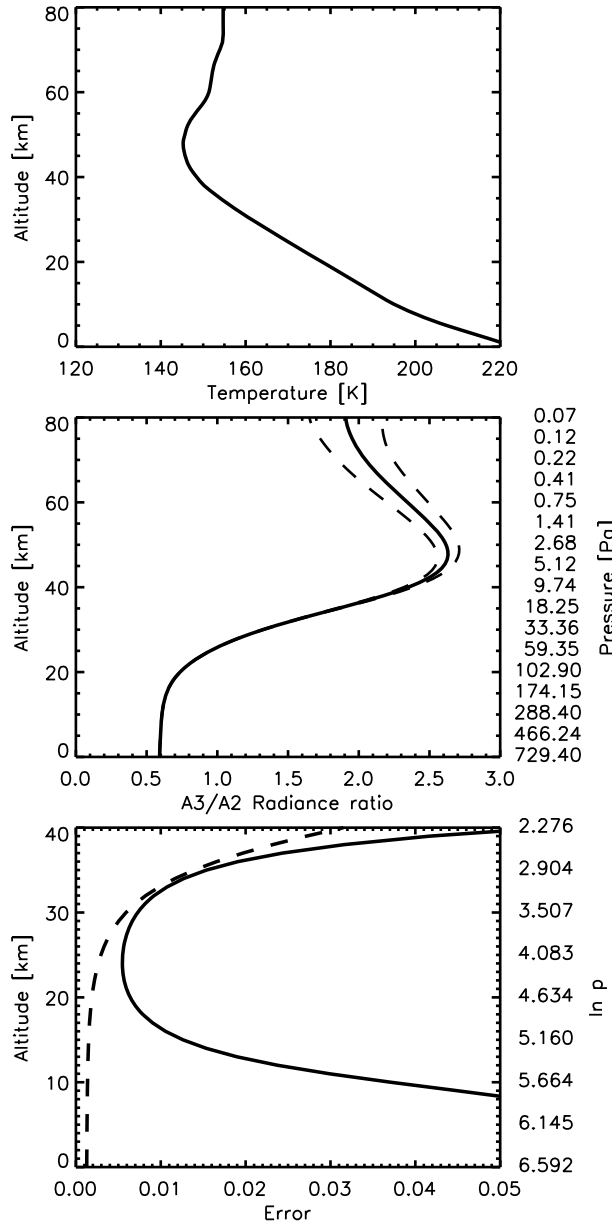
[53] A first guess for surface pressure is based on the annual pressure cycle measured by the Viking 1 Lander. We use the fits given by *Tillman et al.* [1993] to calculate surface pressure vs. L_s on a grid of 1° L_s. To find a first guess we interpolate the surface pressure to the L_s of the measurement, and adjust it for surface elevation using the hydrostatic equation on the atmospheric temperature first guess.

[54] For dust it was determined that a homogeneously mixed profile for low dust conditions (nadir optical depth of 0.2 in the visible or about 0.045 in the infrared at 463 cm^{-1}) served well as a first guess. For ice it was decided to use a constant extinction profile with low but nonzero extinction. A level of 10^{-5} km^{-1} at 843 cm^{-1} was determined to be appropriate.

3.2.4. Pressure

[55] While the retrieval is performed internally on an altitude grid, the altitude information obtained from the spacecraft pointing cannot be assumed to be more accurate than about 1 km. To be more independent of spacecraft pointing accuracy we retrieve pressure together with temperature, dust and water ice opacity. The latter retrieved quantities are then reported on a pressure grid.

[56] The pressure retrieval is based on the analysis of the ratio of the radiances in the A3 and A2 channels. Channel A3 is located in the center of the 15 μm CO$_2$ band while channel A2 is located off center. The ratioing of the

Figure 6. (top) Northern midlatitude summer temperature profile used for sensitivity study. (middle) Ratio of the radiances calculated for the A3/A2 channels. The dashed lines give the error in the radiance ratio due to noise. They have been calculated by error propagation from the values in Table 1 for an average of five individual 2-s measurements. (bottom) Fractional error in the radiance ratio (dashed) and fractional error in pressure (solid).

radiances ensures that the extracted information depends primarily on pressure, and is only weakly dependent on the temperature profile. Figure 6 shows the A3/A2 radiance ratio calculated for a northern midlatitude summer temperature profile. In the lowest 20 km both channels are essentially opaque, leading to a nearly constant radiance ratio. Between 20 and 40 km channel A2 becomes increasingly transparent while A3 stays essentially opaque, leading to a slope in the radiance ratio. From this region the information on pressure can be extracted. Above ~40 km

both channels become transparent such that the ratio changes characteristics again. In addition, above ~50 km detector noise starts to have a noticeable influence on the uncertainty of the ratio. Figure 6 (bottom) gives the fractional error in the radiance ratio due to noise. It increases with altitude and becomes larger than 1% at about 30 km. The solid line in the same plot gives the fractional error in pressure corresponding to the error in radiance ratio, which corresponds to the fractional error in pressure. The pressure error does not only depend on noise but also on the slope of the radiance ratio profile. Hence this error tends to be high in the lower atmosphere as there is little change in radiance ratio with pressure. For a midlatitude summer temperature profile we see a minimum of the fractional error in pressure between 20 and 30 km altitude. In this region we expect a sensitivity to pressure of better than 1%.
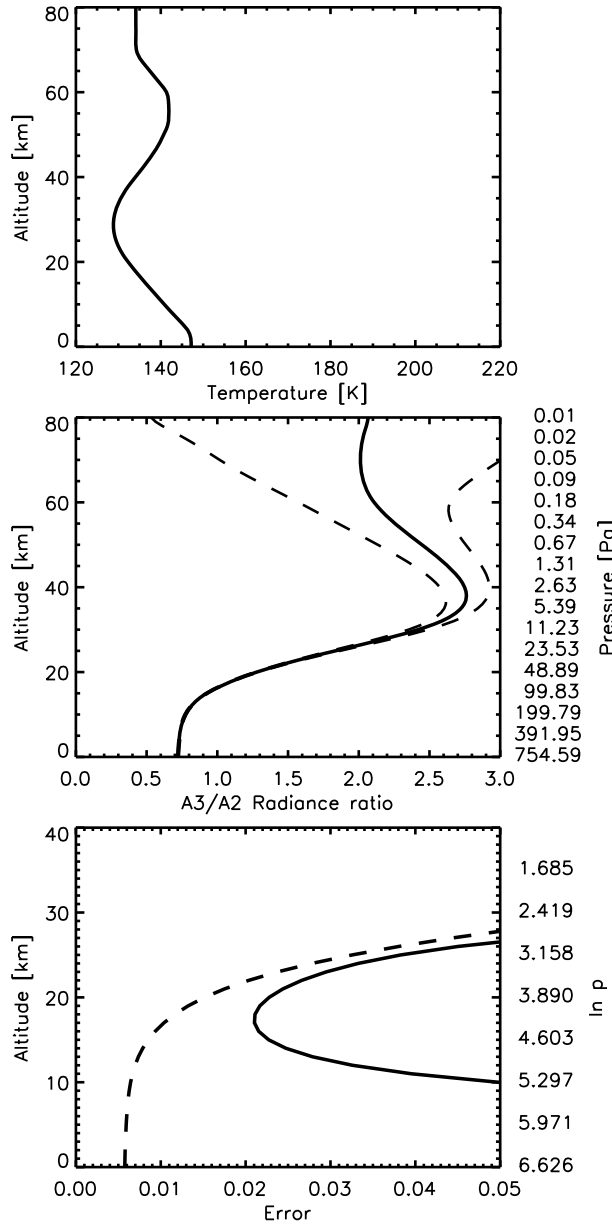
[57] Figure 7 shows a similar sensitivity study for a southern polar winter profile. The much colder temperatures lead to lower radiances and reduced altitudes for pressure levels. In turn the slope in radiance ratio starts to develop at 10–15 km altitude, and the uncertainty of the ratio due to noise becomes obvious at 30 km altitude in Figure 7 (middle). Figure 7 (bottom) shows that the fractional error in radiance ratio exceeds 1% at 20 km, and 5% at 30 km. Hence the region in which the retrieval is sensitive to pressure is lower in altitude, centered at ~17 km, and much narrower than in the midlatitude summer case. We cannot expect a precision of better than 2% in such a cold atmosphere.

[58] To setup a pressure retrieval, the algorithm uses the measured radiances in the A3 and A2 channels together with the pointing geometry to estimate a target altitude for which the retrieval is to be performed. A pressure profile versus altitude is calculated hydrostatically from the first guesses of surface pressure and atmospheric temperature profile. The target altitude is defined as the altitude at which the minimum fractional error in pressure is to be expected. The retrieval selects the A3 and A2 detectors pointing closest to this target altitude, and the ones directly above and below. Radiances and radiance ratios are calculated for the selected detectors. The pressure profile is scaled using a scale factor based on the square of the ratio of the calculated and measured radiance ratios in each A3/A2 detector pair, weighted by the inverse square of the expected error in the logarithm of pressure for each detector pair:

$$s_r = \left(\sum_{i=1}^{3} \frac{(r_{c,i}/r_{m,i})^2}{n_i^2} \right) \bigg/ \sum_{i=1}^{3} \frac{1}{n_i^2}. \qquad (33)$$

[59] Here s_r is the scale factor, $r_{c,i}$ and $r_{m,i}$ are calculated and measured radiance ratios for A3/A2 detector pair i, respectively, and n_i is the error in the logarithm of pressure due to noise for detector pair i.

[60] It was discovered that the assumption of horizontal homogeneity within an altitude layer could cause problems with the pressure retrieval in regions where this assumption is not very good, e.g., at the edge to the polar night where strong horizontal temperature gradients can exist in the atmosphere. The pressure retrieval is particularly sensitive to this issue as it relies on a radiance ratio between a channel that is opaque and a channel that is transparent. While the major part of the radiance in the transparent channel

Figure 7. (top) Southern polar winter temperature profile used for sensitivity study. (middle) Ratio of the radiances calculated for the A3/A2 channels. The dashed lines give the error in the radiance ratio due to noise; calculated in the same way as in Figure 6. (bottom) Fractional error in the radiance ratio (dashed) and fractional error in pressure (solid).

originates at the tangent point, significant parts of the radiance in the opaque channel are likely to originate from regions closer to the spacecraft and hence from an atmosphere at a different temperature than that seen by the transparent channel. To mitigate this effect an a priori constraint was introduced, on the basis of the deviation of the retrieved pressure from the first guess

$$d = \frac{s_r \cdot p_0 - p_{0,guess}}{p_{0,guess}}. \qquad (34)$$

[61] Here $s_r \cdot p_0$ is the surface pressure that would be obtained in the next iteration of the retrieval without a constraint, and $p_{0,guess}$ is the initial surface pressure guess. A constraint of the form
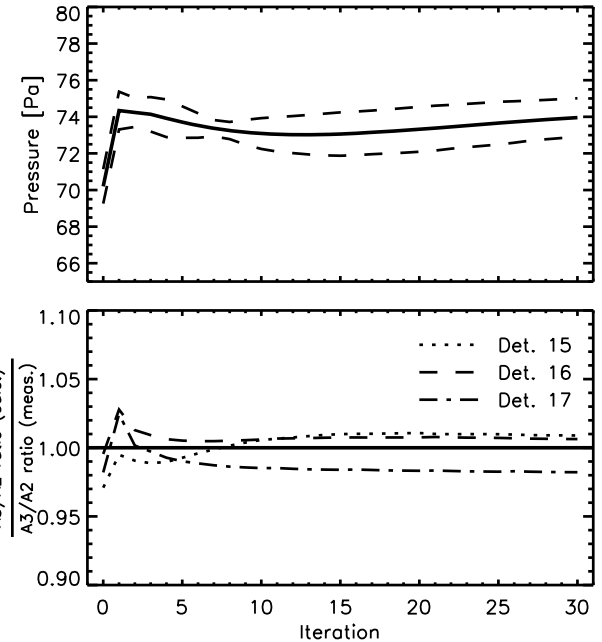
$$c = \frac{1}{1 + (15d)^2} \qquad (35)$$

has very little effect on deviations up to ~15% around the guessed surface pressure but provides a strong restriction as deviations approach 30%. Finally, the scale factor for the pressure retrieval has the form

$$s_p = 1 + (s_r - 1) \cdot c. \qquad (36)$$

[62] This scale factor is applied multiplicatively to the whole pressure profile in one iteration of the pressure retrieval. In the retrieval process the pressure iterations are combined with iterations in temperature, dust, and water ice.

[63] Figure 8 shows the development of retrieved pressure over 30 iterations for a measurement example in the northern midlatitude summer at the location given in Table 3 (in the following termed as measurement 1). The pressure is given for a target altitude of 24 km. The guessed pressure (iteration 0) is already close to the retrieved pressure and most of the distance is covered in the first iteration. Figure 8 (bottom) shows the fit to the measured radiance ratio for the A3/A2 pairs of detectors 15, 16, and 17. The fit is already close at the start of the retrieval, and improves in the first few iterations. The error bars for the retrieved pressure are calculated as a root-sum-square (RSS) from the noise in the radiance ratios and the quality of the fit to the radiance

Figure 8. (top) Retrieved pressure at a target altitude of 24 km for measurement 1 in Table 3. Dashed lines indicate error bars. (bottom) Calculated A3/A2 radiance ratios divided by measured A3/A2 radiance ratios; different line types indicate the three detector pairs used.

Table 3. Locations of the Measurement Examples Discussed in Section 3.2[a]

	Measurement 1	Measurement 2
Latitude (deg)	57.1	−86.5
Longitude (deg)	−43.8	−51.9
L_s (deg)	159.4	135.5
Local time (MLT)	1520	2135

[a]Measurement 1 is for northern midlatitude summer, and measurement 2 is for southern polar winter.

ratios. Although the fit is reasonable at iteration 30, some inconsistencies seem to exist between the three detector pairs, leading to a pressure error of 1.4%.

[64] Another example of a pressure retrieval is given in Figure 9 for a measurement in the southern polar winter region (measurement 2 in Table 3). The pressure is given for a target altitude of 11 km (note that this altitude is with reference to the surface, which is higher than the areoid by several km in this region). The initial pressure guess is farther away from the retrieved pressure and the initial fit is significantly worse than in measurement 1. The fit improves continuously over the 30 iterations although the most progress is made in the first 10 iterations. The resulting fit is very good and the error in pressure after 30 iterations is calculated to be 2.1%, which is very close to the limit determined by the uncertainty in the radiance ratios due to noise for a cold atmosphere (compare Figure 7).

3.2.5. Temperature

[65] The retrieval of temperature is based on the channels A1, A2, and A3. The A3 channel, which is located in the center of the 15 μm CO_2 band, has the strongest CO_2 absorptions and hence is sensitive to the highest levels of the atmosphere. At altitudes where the CO_2 optical depth in the A3 channel exceeds 2.0 along the line of sight (LOS), the retrieval algorithm replaces A3 detectors with detectors in channel A2. If the CO_2 optical depth also exceeds 2.0 in channel A2 below some altitude, A2 detectors are replaced by A1 detectors. As the detector array is typically pointed such that lines of sight of the lowest two detectors intersect the surface, the lowest A1 detector is required to have a surface contribution of less than 20% in its FOV in the case where the atmosphere is still transparent. In the case where the atmosphere is opaque close to the surface, the lowest A1 detector will be that for which the atmosphere becomes opaque in the detector's LOS, such that the measurement with this detector will have nadir-like characteristics.

[66] The scale factors for the iterative part of the temperature retrieval are based on brightness temperature defined by the inverse Planck function. A scale factor is calculated for each detector i as the ratio of the measured and the calculated brightness temperatures, calculated with a weight based on the optical depth along the LOS of the considered detector such that

$$s_{T,i} = \frac{T_B\left(\nu_c, \frac{R_{m,i}}{1-e^{-\tau}}\right)}{T_B\left(\nu_c, \frac{R_{c,i}}{1-e^{-\tau}}\right)}. \quad (37)$$
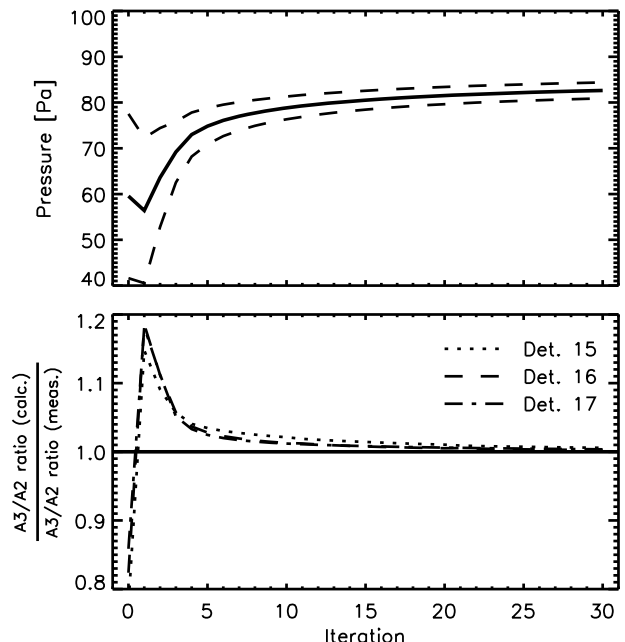
[67] Here $s_{T,i}$ is the scale factor for detector i, ν_c is the center frequency of the channel the considered detector belongs to, $R_{m,i}$ and $R_{c,i}$ are the measured and calculated

radiances, respectively, and τ is the optical depth along the LOS. Radiances are normalized by the approximate limb emissivity $(1 - e^{-\tau})$ before brightness temperatures are calculated. The scale factors for each detector are then combined using the response given by the weighting functions in equation (31), resulting in a scale factor for each altitude level.
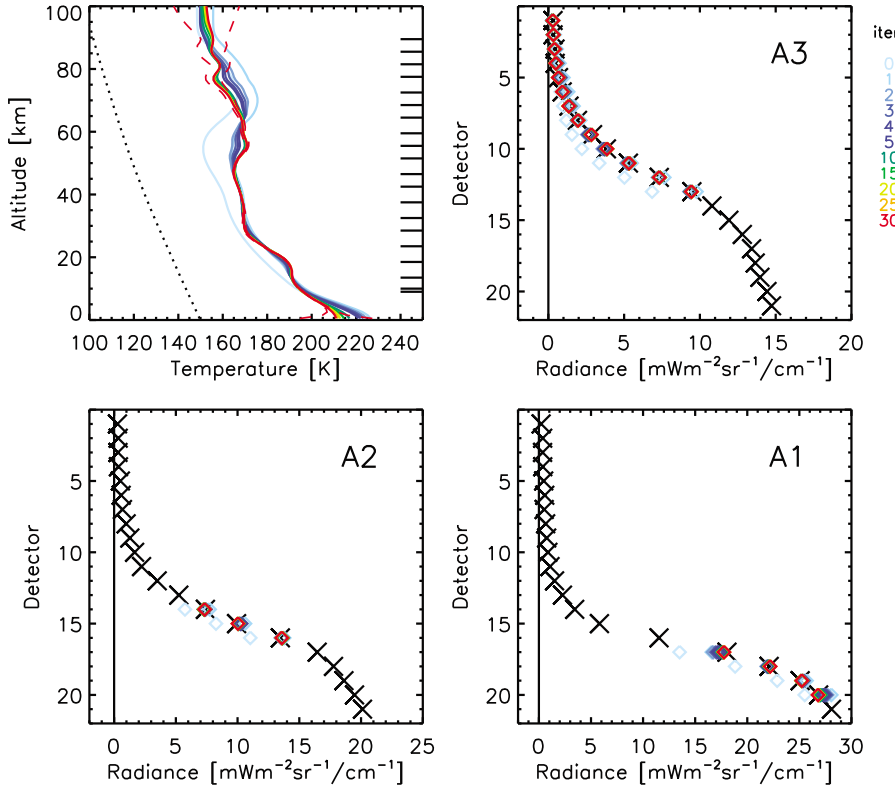
[68] The temperature retrieval is essentially unconstrained. Constraints are only applied at the surface and in the upper atmosphere. A surface constraint adjusts the surface temperature such that the difference between the surface temperature and the retrieved temperature in the lower atmosphere stays the same as in the first guess. In the upper atmosphere the temperature profile progressively relaxes to isothermal above the level where the temperature error is expected to exceed 5%. This limits the influence of noise on the upper atmospheric part of the profile.

[69] After each temperature iteration a 1 km triangular smoothing is performed to eliminate ripples caused by the shape of the weighting functions. In addition, pressure at each altitude level is recalculated using the hydrostatic equation after each iteration to make sure that hydrostatic equilibrium is maintained during the retrieval process.

[70] After the completion of the last iteration, an error estimate for the retrieved temperature profile is performed. The error is calculated from the noise equivalent radiance and the difference between the measured radiance and the calculated radiance for each detector used in the retrieval. We assume that these two quantities are independent and hence use their RSS as our radiance error estimate. To relate the radiance error to an error in the temperature profile we calculate the radiance difference for each detector by perturbing the temperature profile by a constant for each single altitude level. The RSS of the radiance difference due to the perturbed temperature, divided by the radiance error and multiplied by the temperature perturbation for each

Figure 9. Similar to Figure 8 but for measurement 2 in Table 3 and a target altitude of 11 km.

Figure 10. (top left) Retrieved temperature profiles for measurement 1 in Table 3; color coded for different iterations (the light blue line giving the first guess and the red line giving the final result). The red dashed lines indicate the temperature error calculated for the final result. The dotted line gives the CO_2 frost point. The dashes on the right y axis indicate the altitudes that correspond to weighting function peaks. (top right and bottom) Radiances of measurement 1 (crosses) for the A1, A2, and A3 channels and calculated radiances for detectors used in the retrieval (diamonds); color coded for different iterations.

detector then gives an error estimate in temperature for each altitude level. As the altitude grid oversamples the resolution we divide the temperature error obtained from the single level perturbation by the approximate altitude resolution of the measurement, which in the algorithm we assume to be the vertical distance between the weighting function peaks of the temperature measurement.
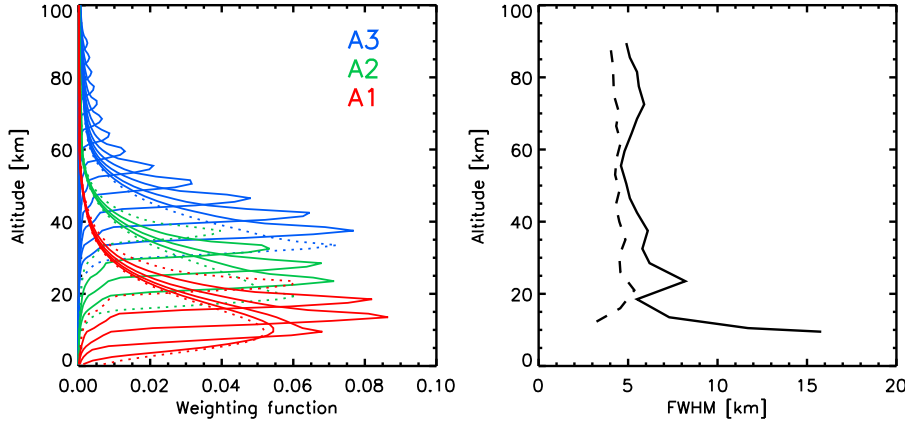
[71] Figure 10 shows the temperature retrieval of the northern midlatitude summer measurement in Table 3 (measurement 1). The detectors used for retrieval cover an altitude range between 10 and 90 km. In the upper middle atmosphere detectors from the A3 channel are used, while in the lower middle atmosphere A2 and in the lower atmosphere A1 detectors are used. The first guess is a typical midlatitude profile. The retrieval converges to a profile very close to the final result within about 10 iterations, and a good fit to the measured radiances in all employed detectors is achieved. Temperature errors are typically around 0.5 K and only increase at low altitudes, where the atmosphere starts to become opaque, and at altitudes above ~60 km, where the signal to noise ratio starts to decrease.

[72] Figure 11 (left) shows the FOV averaged weighting functions of the detectors for the retrieval of measurement 1, color coded for each channel. In addition, weighting functions for detectors that were not used in the retrieval, but are located adjacent to the ones used, are given as dotted lines.

The weighting function gives information on the source altitude for the radiation measured by each detector. Figure 11 (right) shows the full width at half maximum (FWHM) of the weighting functions. The detector selection ensures that the channel is changed from a more opaque to a less opaque channel if the weighting function in the more opaque channel starts to broaden, which would lead to a reduction in altitude resolution. The FWHM of the weighting functions is typically between 5 and 6 km. Around 40 km altitude the weighting functions of the A3 detectors start to become broader, so A2 detectors are used below this altitude. The same thing happens to A2 detectors around 25 km, below which the algorithm switches to A1 detectors. At even lower altitudes the A1 weighting function starts to broaden, until it has the shape typical for a nadir measurement at 10 km, with an FWHM of 10–15 km.

[73] The dashed line in Figure 11 (right) indicates vertical distance between the peaks of the weighting functions. It is mainly determined by the viewing geometry, ~4 km at high altitudes because the tangent point of the LOS is close to the spacecraft, and ~5 km at lower altitudes as the tangent point is farther away. Weighting function separation sets a practical lower limit for vertical resolution. The true altitude resolution lies between this limit and the FWHM of the weighting functions.

[74] To illustrate the effect of horizontal averaging that occurs because of the limb geometry Figure 12 shows
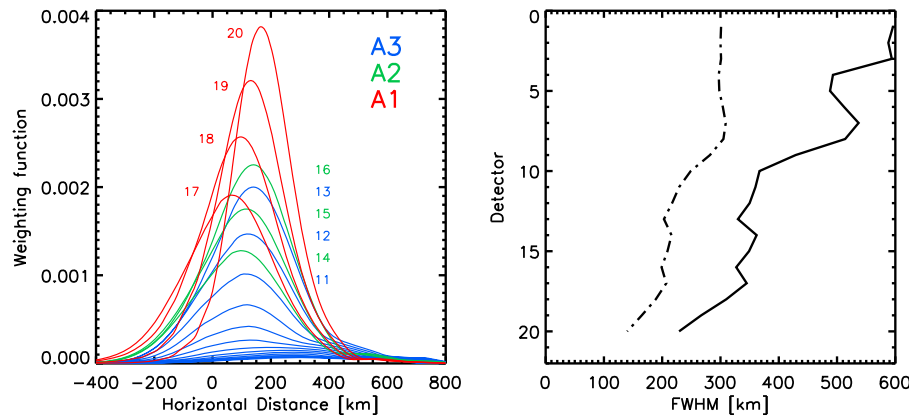
Figure 11. (left) Field-of-view averaged weighting functions for detectors used in the temperature retrieval of measurement 1 (solid) and weighting functions for unused detectors adjacent to the ones used (dotted). The color coding indicates the channel. (right) Full width at half maximum of the weighting functions (solid) and vertical distance between the peaks of the weighting functions (dashed).
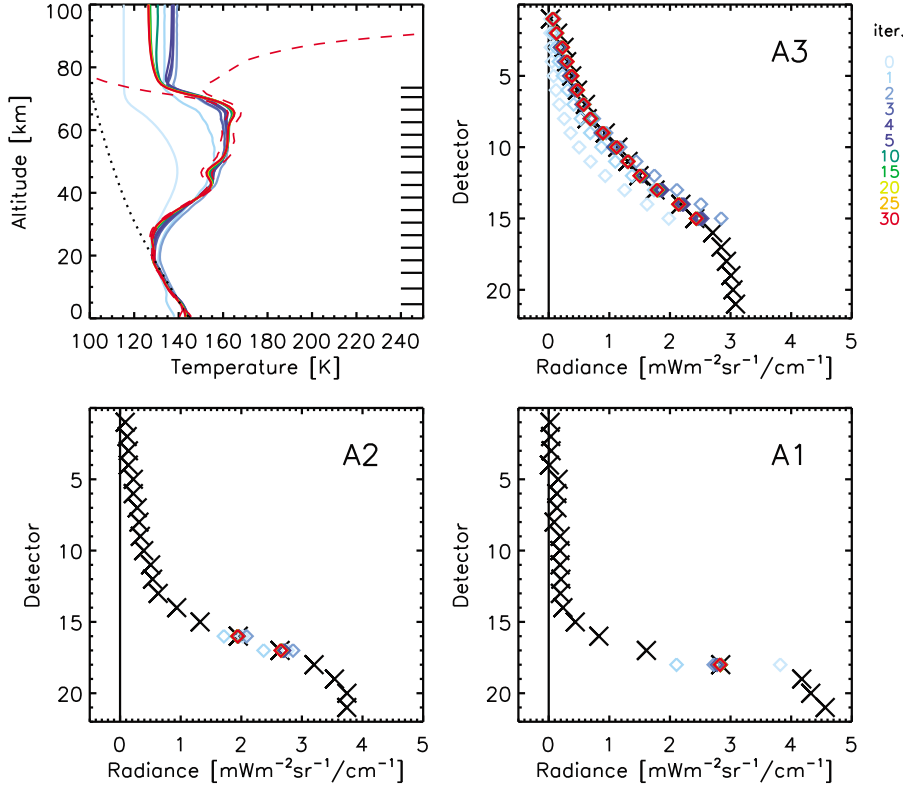
horizontal weighting functions for the detectors used in the temperature retrieval of measurement 1. The origin of the horizontal distance is defined as the tangent point of the boresight of the MCS detector array, roughly corresponding to tangent point of the LOS of detector 11. Distance between the tangent point and the spacecraft is counted positively, while distance beyond the tangent point and away from the spacecraft is counted negatively. Most weighting functions do not peak at the actual tangent point but about 100 to 150 km further toward the spacecraft. This is particularly obvious for detector 20 in channel A1 because this detector points at very low altitudes where the atmosphere is essentially opaque. As the atmosphere becomes less opaque in detectors 19, 18, and 17 the weighting function peak moves away from the spacecraft and toward the tangent point. Above detector 17 the retrieval switches to channel A2 which is more opaque than A1, hence the weighting function peak moves toward the spacecraft again. The same behavior is shown at the transition from A2 to A3. At higher altitudes the beyond

detector 11 the weighting functions tend to broaden out and the peak moves toward the spacecraft again. This effect occurs because of significant contributions of strong Doppler-broadened CO_2 lines to the transmission in the A3 channel. These lines cause significant differences in transmission in the top layers of the atmosphere but contribute little to the weighting function in the lower layers as they become quickly saturated. Note that for the channels A4 and A5, which are used in the water ice and dust retrievals, the weighting functions should be more centered on the tangent point as the opacities in these channels are typically lower, and they have no significant contributions from strong Doppler lines.

[75] Figure 12 (right) shows the widths of the horizontal weighting functions. The width is smallest in the lower atmosphere, when significant atmospheric opacity is present, and becomes larger in the higher atmosphere. The width of the area corresponding to an emissivity of 50%, a measure for the horizontal resolution of the measurement, is shown as a dash-dotted line in Figure 12. In the lower

Figure 12. (left) Field-of-view averaged horizontal weighting functions for detectors used in the temperature retrieval of measurement 1. The color coding indicates the channel, and the numbers give detector numbers for selected detectors. (right) Full width at half maximum of the horizontal weighting functions (solid) and width of the area corresponding to an emissivity of 50% (dash-dotted).
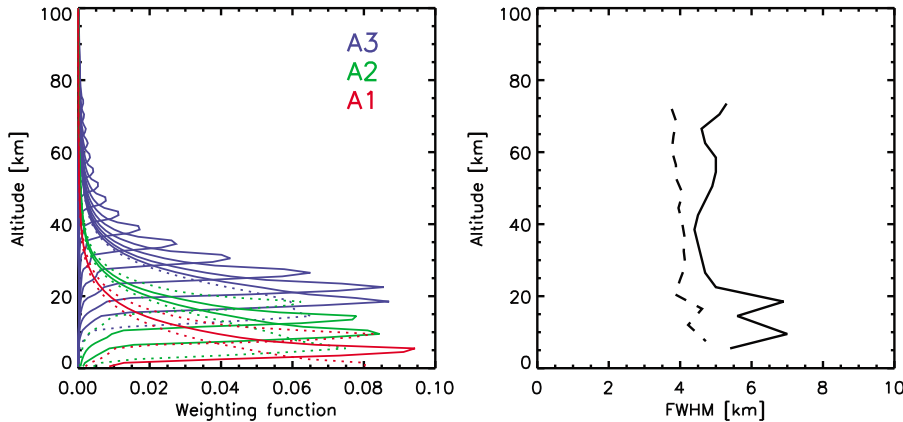
Figure 13. As in Figure 10 but for measurement 2 in Table 3.

atmosphere 50% of the emissivity originates along a path of ~150 km, while higher in the atmosphere 50% of the emissivity originates along a 300 km range.
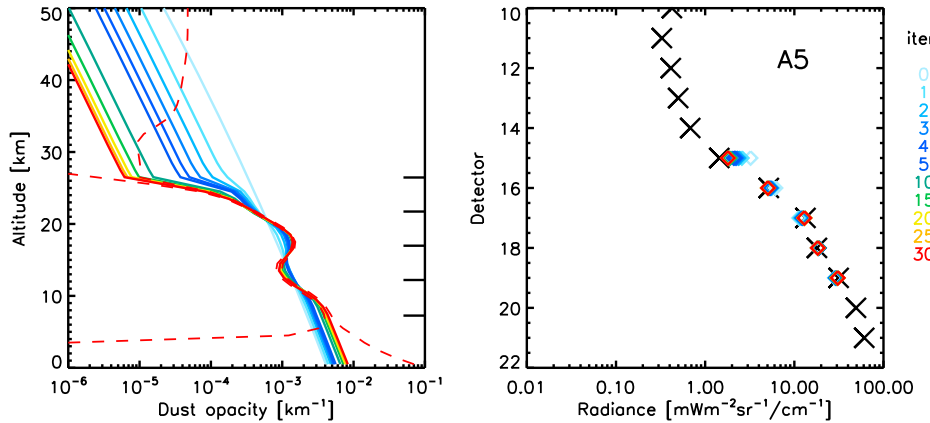
[76] Figure 13 shows the temperature retrieval of the southern polar winter measurement in Table 3 (measurement 2). Here the detectors cover an altitude range between 5 and 75 km. Detectors from channel A3 are used down to 20 km, a much lower altitude than in measurement 1. Only one detector of the A1 channel is used close to the surface as atmospheric opacity falls rapidly with temperature in channels A1 and A2. The first guess is a typical polar winter profile exhibiting a warming in the middle atmosphere. The final profile also shows a middle atmospheric warming. However, it is centered at higher altitudes and shows with

~165 K a much larger inversion than the first guess profile. In the lowest 20 km the retrieved profile closely follows the frost point curve of CO_2, although there is no constraint requiring this in the temperature retrieval. Temperature errors are around 0.5 K at low altitudes, rising to >1 K above 40 km and to >3 K above 65 km as the atmosphere is very cold at these altitudes.

[77] Figure 14 shows the weighting functions of the detectors for the retrieval of measurement 2, together with their FWHM and the vertical distance between their peaks. The vertical distance between the weighting function peaks is around 4−5 km, similar to measurement 1. The FWHM of the weighting functions of the A3 detectors is around 5 km down to an altitude of 25 km. At 20 km altitude it

Figure 14. As in Figure 11 but for measurement 2 in Table 3.

Figure 15. (left) Retrieved dust opacity profiles for measurement 1 in Table 3; color coded for different iterations. The red dashed lines indicate the dust error calculated for the final result. The dashes on the right y axis indicate the altitudes that correspond to weighting function peaks. (right) Radiances of measurement 1 (crosses) for the A5 channel and calculated radiances for detectors used in the retrieval (diamonds); color coded for different iterations.

broadens to 7 km so that the A2 channel is used around 10–15 km. Note that the A1 detector which is used around 5 km altitude is not opaque, so that we achieve an altitude resolution of ~5 km in these cold polar conditions even in the lowest part of the atmosphere.

3.2.6. Dust

[78] Channel A5 is used for the retrieval of dust opacity. The selection of A5 detectors is based on several criteria. The lowest detector used for retrieval is required to have a surface contribution of less than 10% in its FOV and an optical depth along the LOS of less than 2.5. The latter criterion is a reasonable cutoff to prevent the analysis of radiance data where the limb is too opaque to provide useful information for a profile retrieval. The highest detector used for retrieval is required to have a radiance of at least 5% of the maximum radiance of any detector in the A5 channel. This ensures that small misrepresentations of FOV wings in detectors with very low radiances do not get interpreted as dust by the retrieval.

[79] The scale factors for the dust retrieval are based on the ratio between the measured and calculated radiances in the A5 detectors of the form

$$s_{d,i} = 1 + \frac{R_{m,i} - R_{c,i}}{R_{c,i}} \cdot e^{-\tau}. \tag{38}$$

[80] Here $s_{d,i}$ is the scale factor for detector i, $R_{m,i}$ and $R_{c,i}$ are the measured and calculated radiances, respectively, and τ is the optical depth along the LOS. In the optically thin limit, this scale factor is $R_{m,i}/R_{c,i}$. In the optically thick limit, it tends to unity. The scale factor for each detector is then distributed over the dust opacity profile using the weighting functions as described in equation (31).

[81] For altitude levels below the peak of the lowest weighting function as well as above the peak of the highest weighting function the dust opacity is extrapolated in proportion to pressure, which corresponds to a constant mixing ratio. However, these altitude levels are not reported as retrieval results. Smoothing is performed to eliminate ripples caused by the shape of the weighting functions.
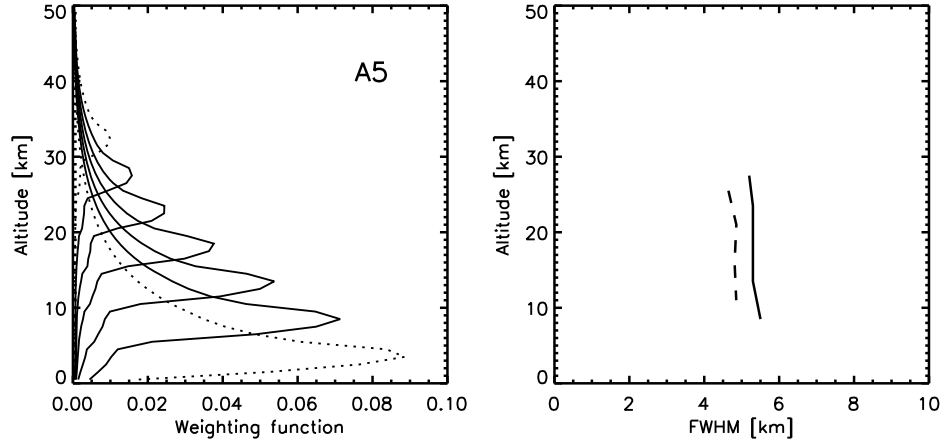
[82] After the last retrieval iteration, an error estimate for the retrieved dust opacity profile is performed. To calculate an error profile for dust opacity by means of a single level perturbation, it would require a full radiative transfer calculation for each altitude level. This would be very time consuming, hence a simplification is applied. We calculate a radiance difference from a dust profile perturbed by a constant factor at all altitude levels. We use this radiance difference profile multiplied by a normalized weighting function for each detector at each altitude level as a substitute for a single level perturbation. This quantity is then used to estimate the precision at each altitude level from the RSS of the noise equivalent radiance and the quality of the fit, analogously to the estimate of temperature precision. This approach gives reasonable agreement (typically within ~20%) with error bars calculated using an exact single level perturbation, when significant dust opacity is present.

[83] Figure 15 shows a dust retrieval for a northern midlatitude summer measurement (measurement 1 in Table 3, no significant dust was retrieved for measurement 2). Five detectors in the A5 channel are selected for retrieval, covering an altitude range between 8 and 26 km. The dust profile of the initial guess is homogeneously mixed. As the retrieval progresses the dust at lower altitudes stays close to homogeneously mixed, while at higher altitudes the dust profile starts to flatten significantly, indicating a fairly clear area above the highest detector used in the retrieval.

[84] In Figure 16 the detector weighting functions for the dust retrieval of measurement 1 are shown, together with their FWHM and the vertical distance between their peaks. The vertical distance between the weighting function peaks is 4.5–5 km, while the FWHM of the weighting functions is 5–5.5 km. Detector selection ensures that the atmosphere in the retrieved altitude range does not become sufficiently opaque to degrade the altitude resolution of the dust retrieval, which is about 5 km.

3.2.7. Water Ice

[85] The retrieval of water ice is based on channel A4. A comparison of calculated radiances with averaged measured

Figure 16. (left) Field-of-view averaged weighting functions for A5 detectors used in the dust retrieval of measurement 1 (solid) and weighting functions for unused detectors adjacent to the ones used (dotted). (right) Full width at half maximum of the weighting functions (solid) and vertical distance between the peaks of the weighting functions (dashed).

radiances in this channel suggests that the far wings of the FOV at high altitudes seem to be underestimated in the calculation for this channel (JTS). To correct for this we subtract 80% of the radiance in the top A4 detector from the radiances of all detectors in the A4 channel. Analogous to the dust retrieval the lowest detector used in the water ice retrieval is required to have a surface contribution of less than 10% in its FOV and an optical depth along the LOS of less than 2.5. In addition, the selection of the lowest detector for ice is coupled to the selection of the lowest detector for dust such that both dust and ice retrievals have the same lower-altitude bound. The highest detector used for retrieval is required to have a radiance of at least 1%–3% of the maximum radiance of any detector in the A4 channel. The top detector used in the ice retrieval is independent of the top detector used in the dust retrieval.

[86] The scale factors for the water ice retrieval are defined analogous to the dust retrieval

$$s_{h,i} = 1 + \frac{R_{m,i} - R_{c,i}}{R_{c,i}} \cdot e^{-\tau}, \qquad (39)$$

where $s_{h,i}$ is the scale factor for detector i, $R_{m,i}$ and $R_{c,i}$ are the measured and calculated radiances in the A4 detectors, respectively, and τ is the optical depth along the LOS for each detector. The scale factor for each detector is then distributed over the water ice profile using the response given by the weighting functions as described by equation (31).

[87] To accommodate the more layer-like character that is expected for water ice in the Martian atmosphere we use the tail of a Gaussian both for extrapolating to altitude levels below the peak of the lowest weighting function and above the peak of the highest weighting function. These extensions are only used in the radiative transfer calculations and are not reported as retrieved results. Smoothing is performed to eliminate ripples caused by the shape of the weighting functions. An error estimate analogous to the one for dust is also performed for the water ice retrieval after the last iteration.
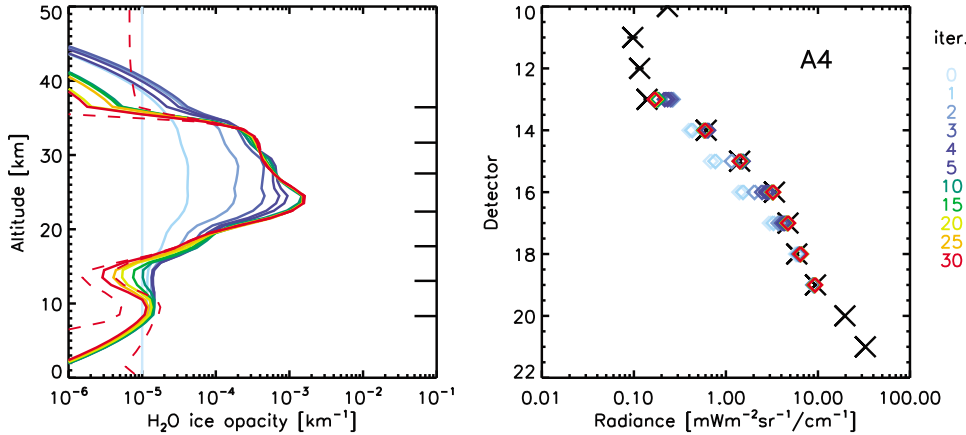
[88] In Figure 17 we see the water ice retrieval for measurement 1 in Table 3 (northern midlatitude summer). For measurement 2 only very low levels of ice were retrieved so no results are shown here. An altitude range between 9 and 37 km is covered by the 7 detectors selected for retrieval. Starting with a constant initial guess the retrieval process shows a roughly 15 km thick ice layer emerging after a few iterations. The bottom of the ice layer is roughly coincident with the top of the dust retrieved from the same measurement.

[89] Figure 18 shows the weighting functions of the detectors used for the water ice retrieval from measurement 1 as well as the FWHM and the vertical distance between their peaks. The vertical distance between the weighting function peaks is 4.5–5 km. The FWHM of the weighting functions is about 5 km at the top of the measurement range, increasing to about 6.5 km at the bottom.

3.2.8. Quality Control

[90] At the end of the retrieval process a quality control is performed. The residuals of the different retrievals (RMS radiance residuals for temperature, dust, and ice retrievals, radiance ratio residuals for the pressure retrieval) are compared with threshold values. If all residuals pass their threshold values a retrieval is considered successful. It was noticed that exceeding the threshold value in one or more retrieved quantities was often related to imperfect fits of detectors pointing close to the surface. If this situation is encountered the residual is recalculated with the lowest detectors omitted. If the threshold is passed retrieved profiles are reported to the lowest altitude covered by detectors.
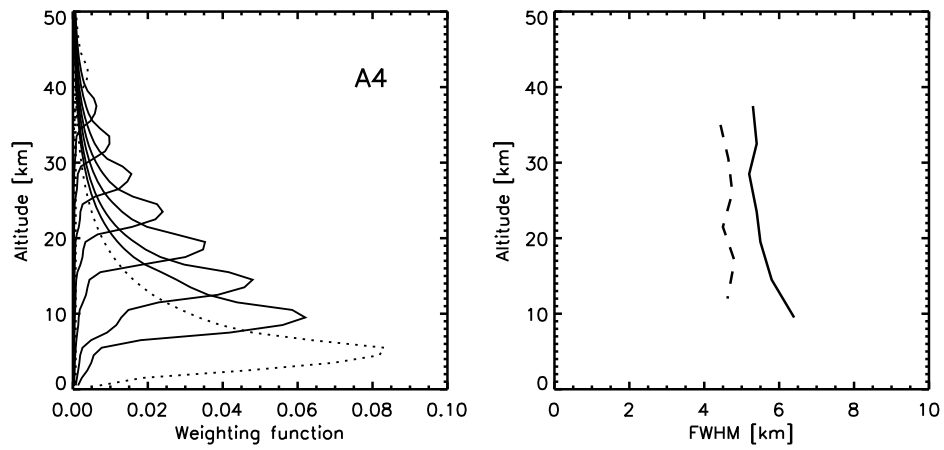
[91] In addition to examining residuals, the retrieved pressure itself is a good indicator of the success of a retrieval. Despite the constraint in the iterative process of the pressure retrieval (equation (35)), the fact that radiance ratios rather than radiances are analyzed makes it very sensitive to inconsistencies. Therefore a retrieval is only selected when the surface pressure, which is extrapolated from the pressure retrieval, is within ±30% of the surface pressure expected from the Viking climatology used as a first guess.

Figure 17. (left) Retrieved water ice opacity profiles for measurement 1 in Table 3; color coded for different iterations. The red dashed lines indicate the water ice error calculated for the final result. The dashes on the right y axis indicate the altitudes that correspond to weighting function peaks. (right) Radiances of measurement 1 (crosses) for the A4 channel and calculated radiances for detectors used in the retrieval (diamonds); color coded for different iterations.

[92] Furthermore retrievals are not reported if the retrieved water ice opacity exceeds 0.004 km^{-1}. Opacities of this magnitude in a layer of significant thickness lead to significant line-of-sight optical depth in the A4 channel. High LOS optical depths in a channel reduce the leverage of the retrieval scale factors (compare equation (39)), which can result in the erroneous interpretation of water ice as dust by the retrieval, when it tries to fit radiances in the A5 channel. The cutoff ensures that spurious dust retrievals in the presence of high ice opacities stay below a few percent of the ice opacity. Retrievals of higher ice opacities will require the use of different channels (e.g., B2), which will be implemented in the future. We note that because of these selection criteria, coverage of successfully retrieved profiles will vary with region and season. Subsequent improvements to the retrieval algorithm will result in a larger and more homogeneous retrieval coverage.

[93] The neglect of scattering in the radiative transfer calculations represents a caveat in the results in conditions with high dust and/or ice opacities. However, with the assumed size distributions dust is fairly black in channel A5 in which it is retrieved, having a single scattering albedo (SSA) of 0.13. The same is the case for water ice in the A4 channel with an SSA of 0.16. Scattering by water ice in channel A5 is not important because of its low extinction efficiency. However, dust scattering in the A4 channel might be an issue as its SSA at this frequency is 0.58 and the dust extinction efficiency is comparable to the ice extinction efficiency in this channel. Significant amounts of dust may not be represented accurately in the radiative transfer of the A4 channel and thus may lead to erroneous features in the ice retrieval. In the case of similar opacities of dust and water ice about 30% of the radiation in the A4 channel originates from scattering. As we are not confident

Figure 18. (left) Field-of-view averaged weighting functions for A4 detectors used in the water ice retrieval of measurement 1 (solid) and weighting functions for unused detectors adjacent to the ones used (dotted). (right) Full width at half maximum of the weighting functions (solid) and vertical distance between the peaks of the weighting functions (dashed).

in the accuracy of an absorption only model in situations with scattering contributions this high we do not report water ice opacities at levels where dust opacity is greater than ice opacity.

[94] Another effect of neglecting scattering is that CO_2 ice cannot be retrieved because CO_2 ice has a very high single scattering albedo at most wavelengths [*Hansen*, 1997]. As CO_2 ice is expected to be present in the polar winter region [*Zuber et al.*, 1998], we suspect that small dust opacities retrieved in some areas of the polar winter region might actually be related to CO_2 ice. We hence decided not to report ice and dust opacities if the temperature is close to the CO_2 frost point, using a criterion of 150 K in the lowermost atmosphere as a threshold. Because the potentially spurious opacities tend to be small we still have confidence in the temperature retrieval performed in these regions.

3.3. Delivery to Planetary Data System

[95] The retrieved profiles that pass the quality control have been delivered as Level 2 (version 1.2.x) data products to the atmosphere node of the Planetary Data System (URL: http://pds-atmospheres.nmsu.edu/).

[96] The Level 2 data files typically comprise the profiles retrieved from 4 h of MCS observations. The content is divided in two structures. The first structure gives auxiliary information such as date, time, local time, solar zenith angle, location, surface and areoid radii. Furthermore it contains several quality flags and information that allows us to identify the radiances that were used to retrieve a particular profile. The second structure consists of 14 columns and 105 lines. Each of the lines corresponds to the level of a regular pressure grid of the structure

$$p_i = p_{ref} \cdot e^{-\frac{i-10}{8}}, \tag{40}$$

where i runs from 1 to 105 and p_{ref} is 610 Pa. This equation creates a pressure grid between $1.8789 \cdot 10^3$ Pa and $4.2470 \cdot 10^{-3}$ Pa, well covering the part of the Martian atmosphere MCS is sensitive to. Note that the pressure grid used by MGS TES is a subset of this grid. Using the retrieved pressure on the internal altitude grid, the retrieved quantities are interpolated onto the regular pressure grid. The natural vertical coordinate is pressure.

[97] The 14 columns contain the following quantities.

[98] 1. The pressure grid in Pa as defined in equation (40) is given.

[99] 2. Temperature and temperature error are the retrieved temperature in K and its precision.

[100] 3. Dust opacity and dust error are the retrieved infrared dust opacity at 463 cm^{-1} in km^{-1} and its precision.

[101] 4. H_2O vapor and H_2O error are the place holder for retrieved water vapor when it becomes available.

[102] 5. H_2O ice opacity and H_2O ice error are the retrieved infrared H_2O ice opacity at 843 cm^{-1} in km^{-1} and its precision.

[103] 6. CO_2 ice opacity and CO_2 ice error are the place holder for retrieved CO_2 ice opacity when it becomes available.

[104] 7. The approximate altitude of the considered pressure level above the surface is reported. Altitude is a relative scale defined independently for each profile. Its accuracy is

determined by limb pointing, and cannot be assumed to be more accurate than ± 1 km.

[105] 8. The approximate latitude of a tangent point at the altitude of the considered pressure level as defined by the limb geometry is given.

[106] 9. The approximate longitude of a tangent point at the altitude of the considered pressure level as defined by the limb geometry is given.

[107] Retrieved quantities are only reported at levels where information on them was actually retrievable from the radiances. At other levels these quantities are marked by a "missing" identifier. The distance in altitude between adjacent pressure levels is typically between 1 and 1.5 km, so the pressure grid is actually oversampling the information in the measurement. Error bars are given as precisions with reference to the actual altitude resolution of the measurement, which is typically about 5 km. Precisions are calculated from the uncertainty due to noise and the quality of the fit, and ignore potential cross correlations like the uncertainty in temperature influencing pressure, or the uncertainty in aerosol influencing temperature.

[108] The accuracy of the data includes the precision but also systematic errors, and hence will be larger than the precision given in the data. Sources of systematic errors include measurement errors, like calibration errors, errors in geometry, or errors in the field-of-view wings. Another source of systematic error is the radiative transfer with errors due to the Curtis-Godson approximation (see section 2.2.3), the neglect of scattering (see section 2.1.2.3), and uncertainties in spectroscopic parameters. As an example, the uncertainty of the line strength of most strong CO_2 lines in the HITRAN database is quoted to be 2–5%, the uncertainty of the self-broadened half width is 5–10% [*Rothman et al.*, 2005]. An error of 5% in one of these quantities translates into an error of about 2% in the calculated radiance, which in turn leads to a temperature error of up to 1 K in a typical midlatitude summer atmosphere. Uncertainties of spectroscopic parameters and size distributions for dust and water ice particles are very difficult to quantify, which should be taken into account when using the data. An initial intercomparison of a temperature profile with measurements from other sources is given in section 6, more validation work will be performed to gain a better insight in the actual accuracy of the data.

[109] Note that the quantities altitude, latitude, and longitude are only approximate and intended to help visualize the location of the retrieved profile, hence no error bars are given for these quantities.

4. Retrieval Simulation
4.1. Approach

[110] To test the retrieval algorithm we perform retrievals from simulated radiances. As an input to the simulation we use the output of the WRF general circulation model [*Richardson et al.*, 2007] as a representation of our current knowledge of the thermal structure of the Martian atmosphere. The output is from a different run than the one used to create first guesses for the retrieval program. In addition, it is sampled at actual locations on the basis of the geometry and timing of MCS measurements, and hence is sufficiently

Table 4. Parameters of the Gaussian Distribution Assumed for the H$_2$O Ice Opacity Profile in the Retrieval Simulation

	South Pole	Equator	North Pole
H$_2$O ice opacity at 843 cm^{-1} at peak altitude (km^{-1})	3 · 10^{-4}	3 · 10^{-3}	8 · 10^{-4}
Peak altitude above surface (km)	10	30	20
FWHM (km)	5	10	5

different from the first guess to perform a meaningful test. Season and observation geometry of the sampled data represent the beginning of the MCS observations (L$_s$ ~ 111°), corresponding to a northern summer/southern winter temperature scenario. To represent the dust distribution we use the dust column as it is parameterized in the model, scale it to a maximum nadir optical depth of 0.5 in the visible (about 0.12 at 463 cm^{-1}) and distribute the opacity in the vertical according to the Conrath profile [*Conrath*, 1975]. We let the Conrath parameter vary with cos(90° minus latitude) such that it has a minimum value of 0.05 at the equator and 0.3 at the poles. As there is no ice in the model output we assume a reasonable distribution by parameterizing its opacity variation with altitude as a Gaussian distribution with the parameters varying smoothly with latitude between the points given in Table 4.
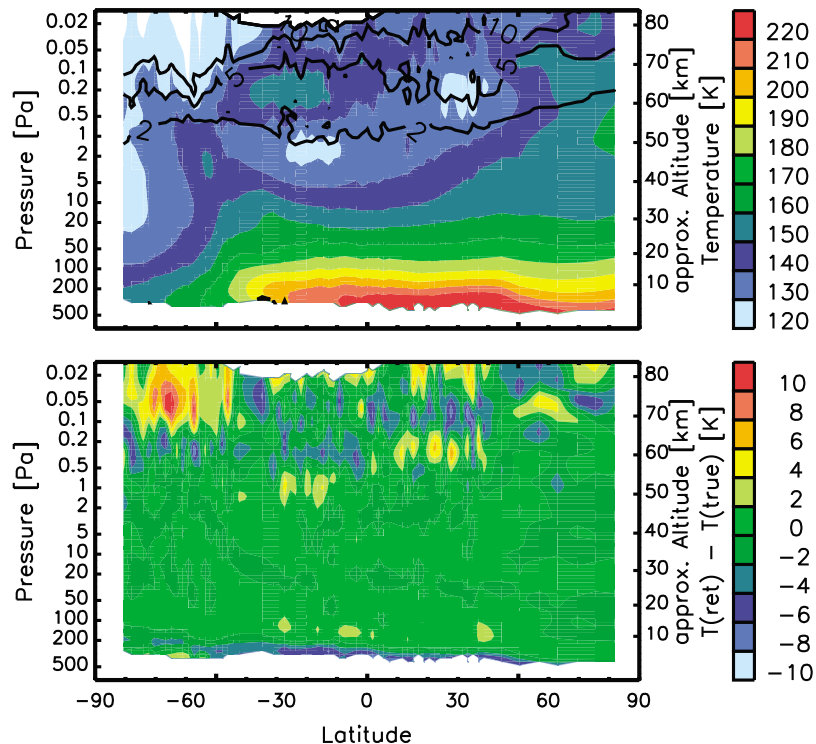
[111] Using the model output and these parameterizations, we perform radiative transfer calculations, add random noise at the level of the instrument performance to the simulated radiances and then retrieve the atmospheric profiles from the simulated radiances using the MCS retrieval algorithm. The aim of the simulation is a detailed comparison of the true and retrieved profiles.
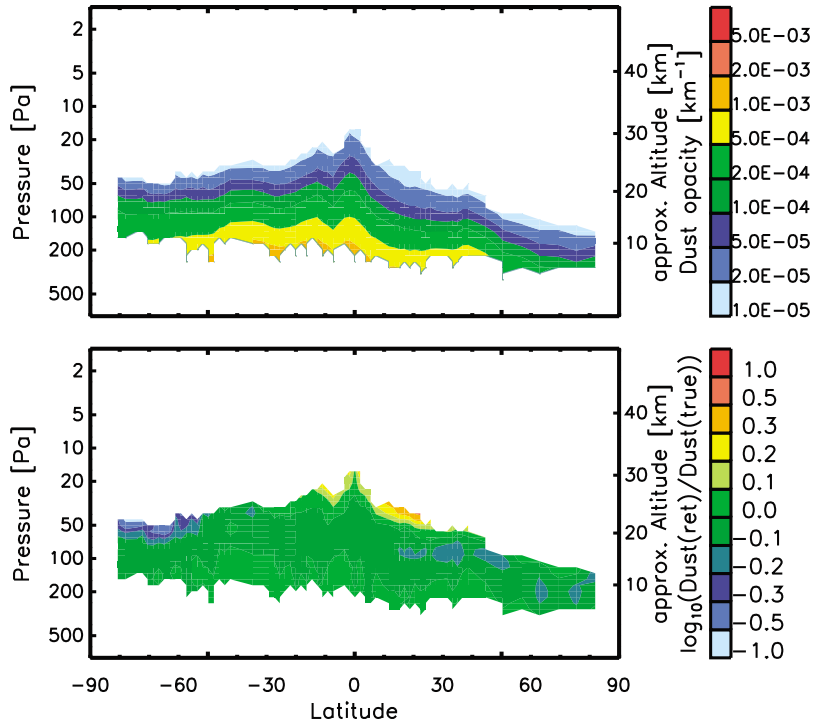
4.2. Simulation Results

[112] Figure 19 shows the result of the temperature retrievals from these simulated data. Figure 19 (top) shows the retrieved temperature structure which corresponds to a northern summer/southern winter atmosphere. Temperatures are fairly homogeneous with latitude and decreasing with altitude in the northern hemisphere. In the southern hemisphere a slight polar warming is apparent, with very low temperatures in the high atmosphere over the south pole. Figure 19 (bottom) shows the difference in temperature between the true temperature used as input for the simulation and the retrieved temperature. The agreement between true and retrieved temperature is very good (below ±2 K) over most of the lower and middle atmosphere up to ~60 km altitude. Differences are slightly larger at low altitudes, as the retrieval cannot be expected to resolve atmospheric structure close to the surface. At high altitudes at equatorial and midlatitudes differences are also slightly larger. This can be attributed to the influence of noise, as the model atmosphere is fairly cold at these altitudes. At high altitudes in the south polar region differences between model temperature and retrieval are rather large. However, the temperature in this part of the atmosphere is very low, leading to retrieval errors of >10 K due to noise, which is consistent with the observed deviations.

[113] Figure 20 shows the dust opacity profiles retrieved from the radiance simulation. Note that a dust profile is only reported at altitudes where detectors were selected for

Figure 19. (top) Retrieved temperatures from a radiance simulation with noise. The solid lines show the retrieved temperature error at the 2, 5, and 10 K levels. (bottom) True temperature subtracted from the retrieved temperature.

Figure 20. (top) Retrieved dust opacities from a radiance simulation with noise. The retrieved dust opacity error is in the order of 10^{-4}–10^{-5} km^{-1}. (bottom) Ratio of the retrieved versus the true dust opacity.

retrieval. At the low end the range is limited by surface contributions or the atmosphere becoming too opaque, at high altitudes it is limited by the lack of radiance suitable for retrieval. Figure 20 (bottom) shows the logarithm of the ratio of retrieved versus true dust opacity. One can see that the retrieved dust is very close to the true dust, with the color code hovering around the zero level (±25%). Only at higher altitudes, where the dust opacity becomes very small (in the order of 10^{-5}) the differences tend to become larger.
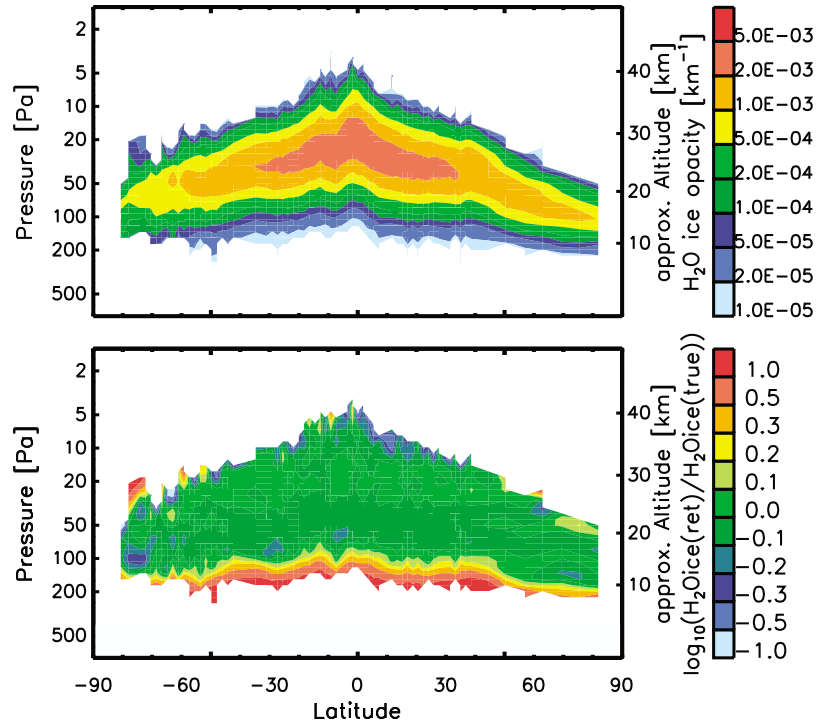
[114] The water ice opacity retrievals from the simulated radiances can be seen in Figure 21. In Figure 21 (bottom) the logarithm of the ratio of retrieved versus true opacity is hovering again around the zero level for most of the retrieved range. Larger differences are only seen at the top and bottom of the altitude ranges covered by the retrievals, where the ice opacity becomes very small. In addition, the results suggest that the retrieval is easily able to distinguish between dust and ice if the relative extinction efficiencies are well known.

4.3. Sensitivity of Retrieval to First Guess
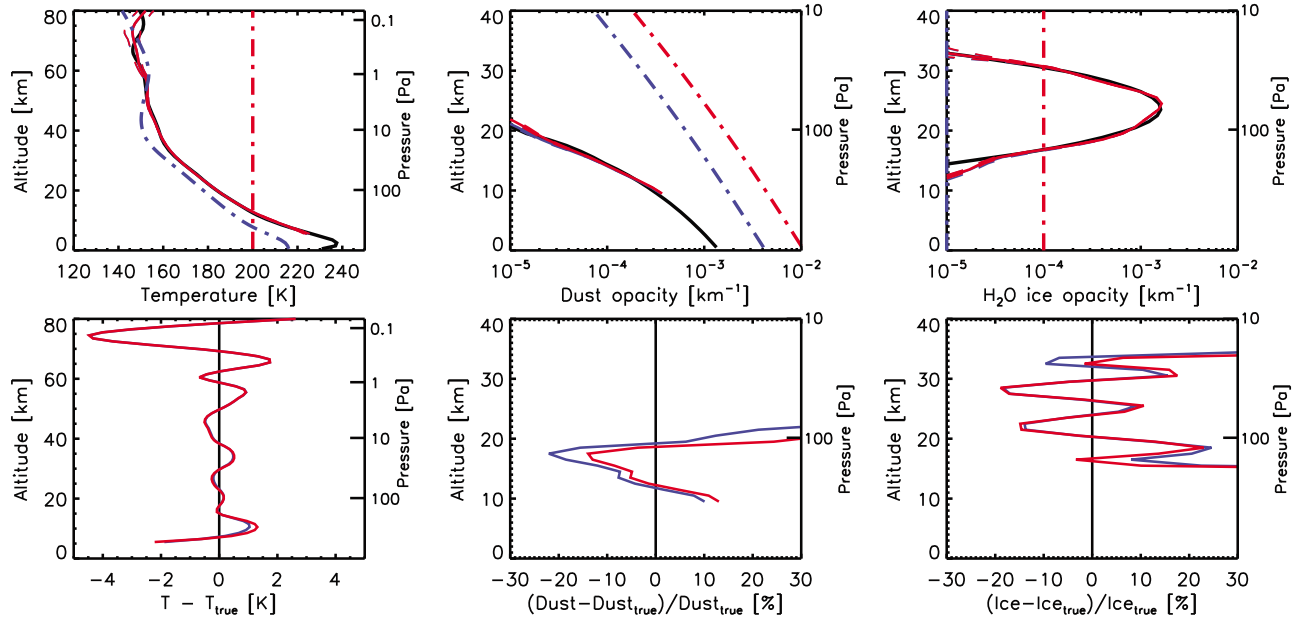
[115] As the sensitivity of a result to the first guess is a general concern for an iterative retrieval method we investigate this issue briefly. We use the retrieval of a case in northern midlatitudes (~55°N) from the simulated data in section 4.2 as an example. Figure 22 shows the true profiles of temperature, dust, and water ice as black lines, the retrieved profiles using the standard first guesses as solid blue lines. Figure 22 (bottom) shows the difference between the retrieved and the true profiles. One can see that the retrieved temperature profile follows the true profile very closely. Only at and below 10 km altitude, where the

atmosphere becomes increasingly opaque, differences up to ~2 K exist. Above ~60 km, where the signal-to-noise ratio starts to decrease noticeably, the retrieval cannot follow the temperature structure as closely either. Differences up to 4 K at ~75 km exist, which are consistent with the retrieved temperature error due to noise at these altitudes. For dust the retrieved profile follows the true profile very closely at altitudes where retrieval results are reported. Only at the upper and lower ends of this range larger differences exist as the retrieval does not quite follow the curvature of the true profile. For water ice a similar situation is observed. The retrieved profile follows the true profile very closely, although differences up to ±25% at individual altitude levels exist. The structure of these differences is related to the position of the individual weighting functions. Considering that the ice profile varies over 2 orders of magnitude within 10 km these effects are to be expected for a measurement with 5 km altitude resolution. Larger differences exist only at the upper and lower ends of the reported altitude range where the ice opacity becomes very small.
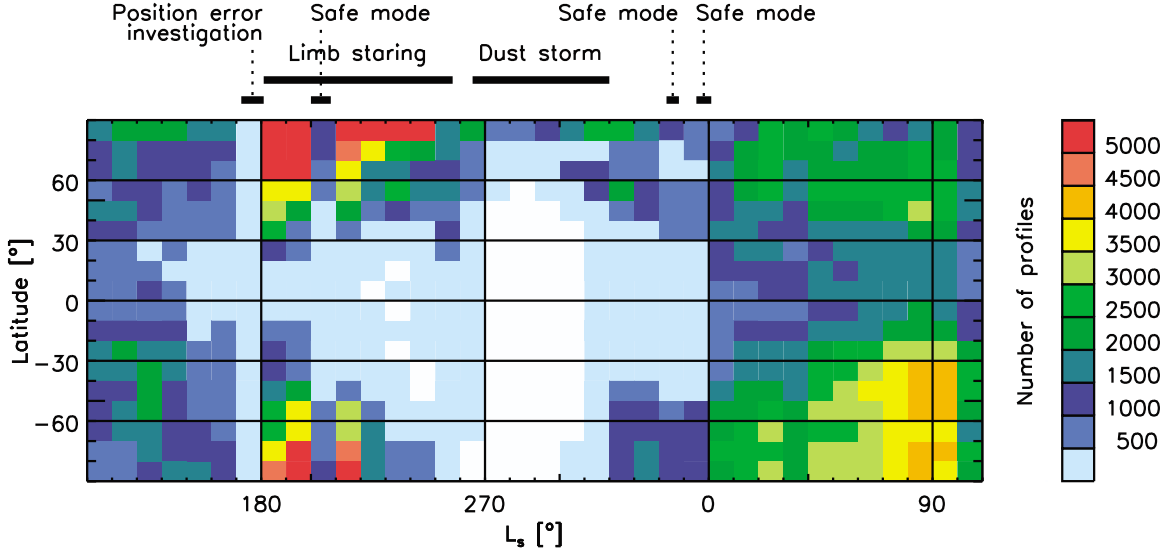
[116] The solid red lines in Figure 22 show retrievals with the first guesses for temperature, dust, and water ice simultaneously modified. For temperature a 200 K isothermal profile was assumed. For dust the original first guess was enhanced by a factor of 2.5, for ice the original first guess was enhanced by a factor of 10. A comparison of these retrievals with the ones that used the original first guesses show that the resulting profiles are very similar. For temperature no significant differences can be seen except around 10 km altitude, where the original retrieval is slightly closer to the true profile. For dust, the modified first guess leads to a profile that is slightly higher than the

Figure 21. (top) Retrieved water ice opacities from a radiance simulation with noise. The retrieved water ice opacity error is in the order of $10^{-4}-10^{-5}$ km^{-1}. (bottom) Ratio of the retrieved versus the true water ice opacity.

Figure 22. Comparison of retrieved profiles from simulated radiances with noise. Black lines show the true profiles, solid blue lines show retrievals with the standard first guess (shown as blue dash-dotted lines), and solid red lines show retrievals with a modified first guess (shown as red dash-dotted line; see text).

Figure 23. Number of retrieved profiles available in version 1.2.x in bins of 10° latitude and 10° L_s for the first MCS year. Times of significant events are marked by bars at the top of the plot.

original retrieval. For ice both results are very similar, even in the structure that is determined by the individual weighting functions. We conclude that the choice of the first guess has only a minimal effect on the retrieval results.

5. Retrieval Results

5.1. Coverage

[117] At the time of writing MCS has been observing for more than 1 Mars year. Retrievals have been performed on most radiance profiles of this data set. Figure 23 shows the availability of retrieved profiles versus latitude and L_s for the first MCS year of observations. It is based on retrievals with the current version of the algorithm (version 1.2.x) described in this paper.

[118] Retrievals are available for most latitudes in most seasons, although the number of retrievals varies depending on instrument operational modes, spacecraft events, and conditions found in the Martian atmosphere. The investigation of position errors of the MCS instrument caused it to be stowed for some time around $L_s = 180°$. Furthermore, the MRO spacecraft experienced three safe mode entries during its first year of operation, which caused MCS to be stowed for several days each time. Figure 23 shows that the number of retrievals is reduced at all latitudes during these times.

[119] During the period when MCS was only staring at the limb, more retrievals than at other times were obtained in many regions. MCS did not take on-planet and calibration measurements during this time, and hence took a limb measurement roughly every 10 s, rather than every 30 s in the standard operational sequence.

[120] Fewer retrievals are found in the equatorial region throughout the Mars year. In the seasons of northern spring and summer high cloud opacities tend to be found between about 10°S and 30°N, reducing the number of successful retrievals. Furthermore dust opacities tend to be particularly high in the equatorial region at all seasons. The addition of channels with lower extinction efficiencies will mitigate these problems in future versions of the algorithm. We note
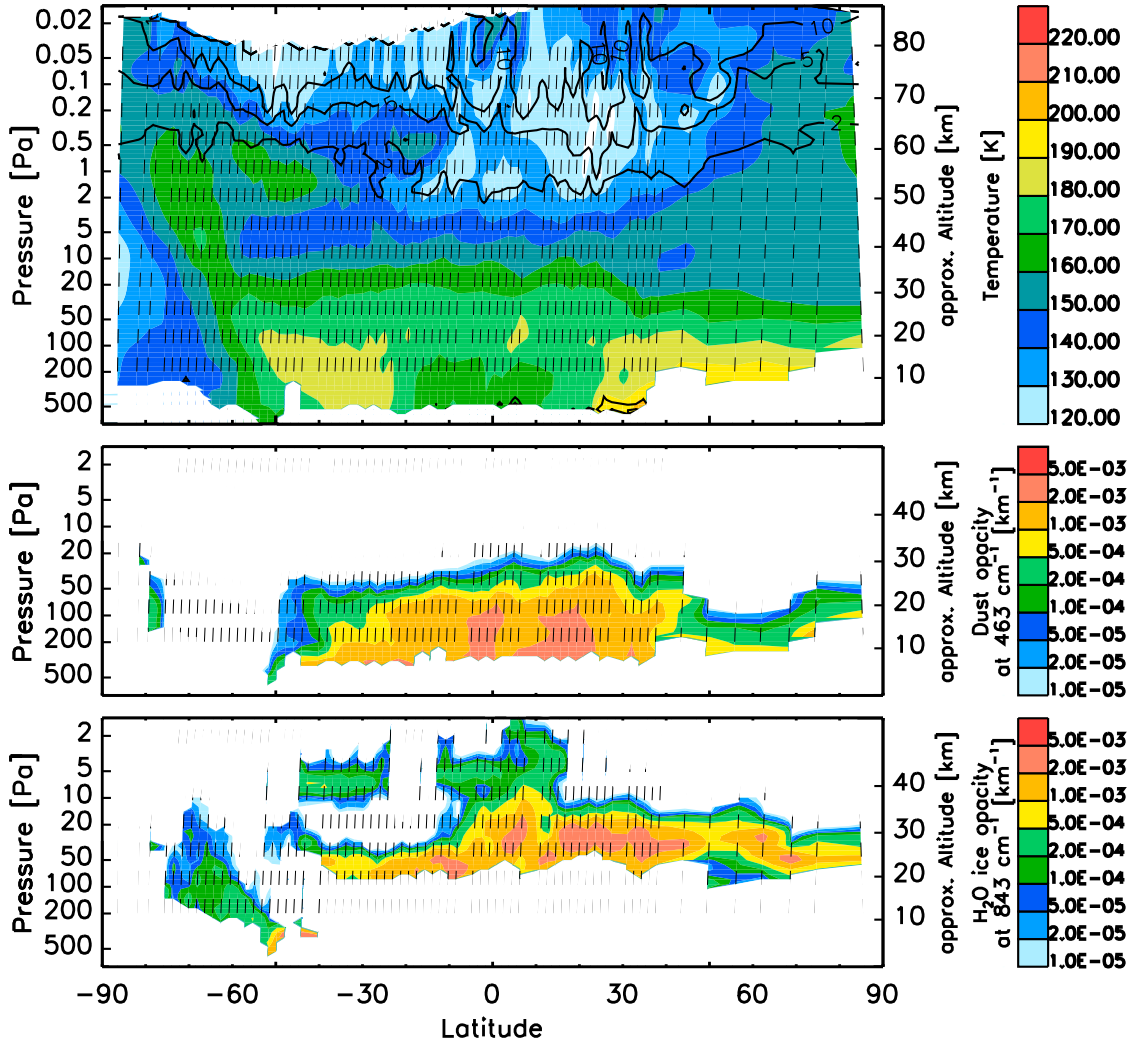
that because of the global dust storm that started around $L_s = 265°$, no limb retrievals were possible over most of the planet. Only in the north polar region, where dust opacities were lower, some profiles could be retrieved.

5.2. Limb-Scanning Period, Northern Summer

[121] In this section we show initial results of retrievals of temperature, dust, and water ice profiles for different phases of the MRO mission. Figure 24 shows a transect of the nighttime side from one orbit at the beginning of the mission ($L_s \sim 111°$), corresponding to northern summer/ southern winter. The temperature structure in the northern midlatitude and polar region is rather homogeneous, with maximum temperatures around 190 K in the lower atmosphere that decrease with altitude to 150−160 K at 10−20 Pa.

[122] The lowest temperatures are found around 0.5 Pa at ~20°N and around 0.1 Pa at 40°−50°S, where temperatures below 130 K are measured. The most striking feature is probably the tongue of warm air extending from 20 to 50 Pa at ~60°S to ~0.5 Pa over the south pole, where temperatures above 170 K are reached despite the fact that most of this region is in polar night. The warming can be attributed to adiabatic heating of the air masses in the downwelling branch of the mean meridional circulation, also termed "Hadley cell" [*McCleese et al.*, 2008]. A similar structure was observed in limb observations by TES [*M. D. Smith et al.*, 2001]. However, the TES retrievals covered only pressures larger than ~1 Pa so they could not observe the decrease in temperature at altitudes above this level. Another temperature maximum, with temperatures above 160 K, is observed at ~50°S around ~1 Pa, which might be related to a secondary circulation cell. Note the minimum with temperatures below 150 K at the 5 Pa level of the same latitude.

[123] Surprisingly low temperatures in the lower atmosphere are retrieved in the equatorial region between 20°S and 20°N at pressures >100 Pa. As this behavior, which was not observed in TES measurements from earlier Mars years at similar seasons [cf. *M. D. Smith et al.*, 2001, Plate 5],
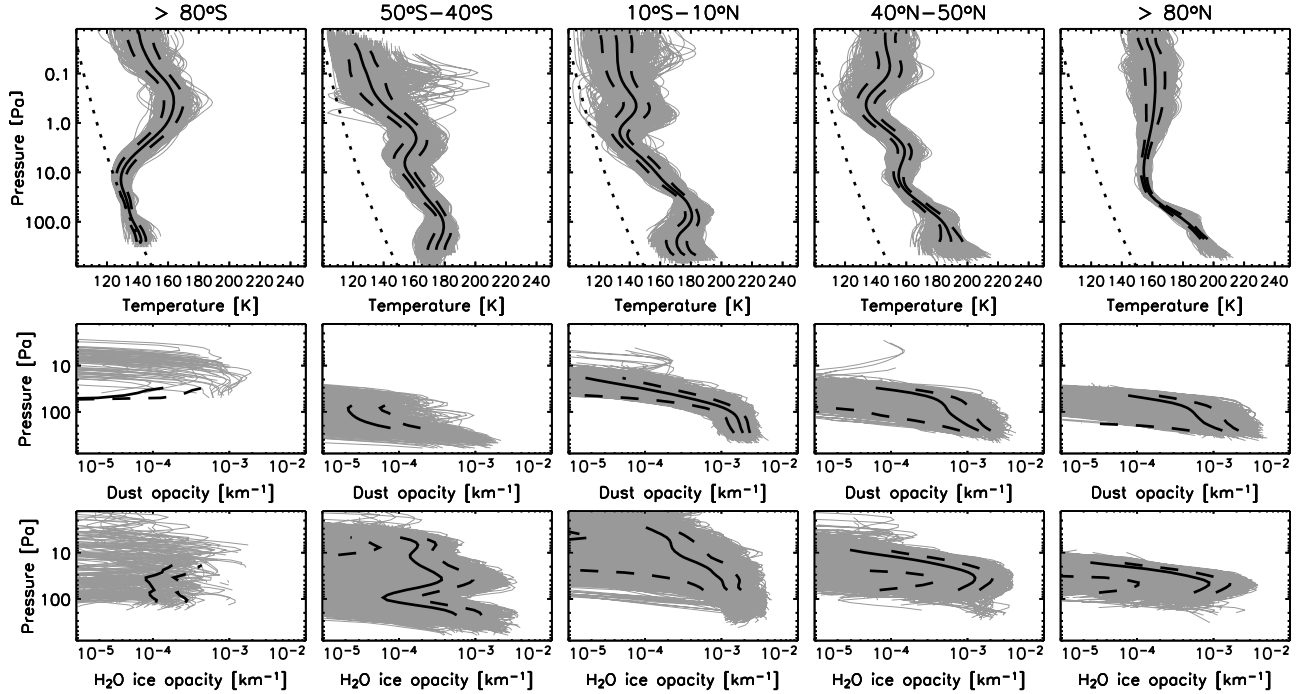
Figure 24. Transect of MCS (top) temperature, (middle) dust opacity, and (bottom) water ice opacity retrievals from an orbit on 25 September 2006 ($L_s = 111°$). The vertical dashed lines mark the latitudinal positions of the tangent points of the individual profile measurements. The solid lines in Figure 24 (top) show the temperature error at the 2, 5, and 10 K levels. Errors for dust and water ice are typically between 10^{-4} and 10^{-5} km^{-1}.

coincides with regions of particularly high aerosol opacities we suspect that it might be caused by the limited representation of aerosols in the current retrieval version. We expect that the inclusion of a scattering parameterization in the radiative transfer and possibly revised particle size distributions will improve the accuracy of the temperature retrieval in the presence of high aerosol opacities in future versions of the retrieval algorithm.

[124] The dust, as shown in Figure 24, seems to be fairly homogeneously distributed with latitude in a band between 30°S and 30°N. North of ~50°N the dust opacities are significantly lower than at equatorial latitudes. Most notable is a region between 50°S and 70°S, where no significant dust opacities were found. This feature seems to be very persistent in this season and forms an annulus around the pole.

[125] The retrieved water ice opacities are shown in Figure 24 (bottom). In this season the aphelion cloud belt is a prominent feature that has been observed in the daytime

[M. D. Smith et al., 2001]. The MCS measurements show that also at nighttime high water ice opacities are found in the equatorial region. The maximum water ice opacity in the MCS retrievals is located above the dust around 20–50 Pa. In addition, significant water ice opacity is observed between 50°S and 70°S at pressure levels of 100–200 Pa. As this region corresponds to the dust free region mentioned above, it is suggestive that scavenging of dust by water ice might have contributed to clearing out this region. An interesting feature is the cloud free stripe that reaches from 10 Pa, ~60°S down to about 200 Pa, ~40°S. This region coincides with the lower part of the warm air tongue that is shown in Figure 24 (top). This suggests that the air downwelling in this region is not saturated. This is most likely due to the adiabatic warming but might also be due to dry descending air not mixing. Another notable feature is the cloud formation at 5 Pa between 45°S and 25°S, which corresponds to the temperature minimum mentioned above.
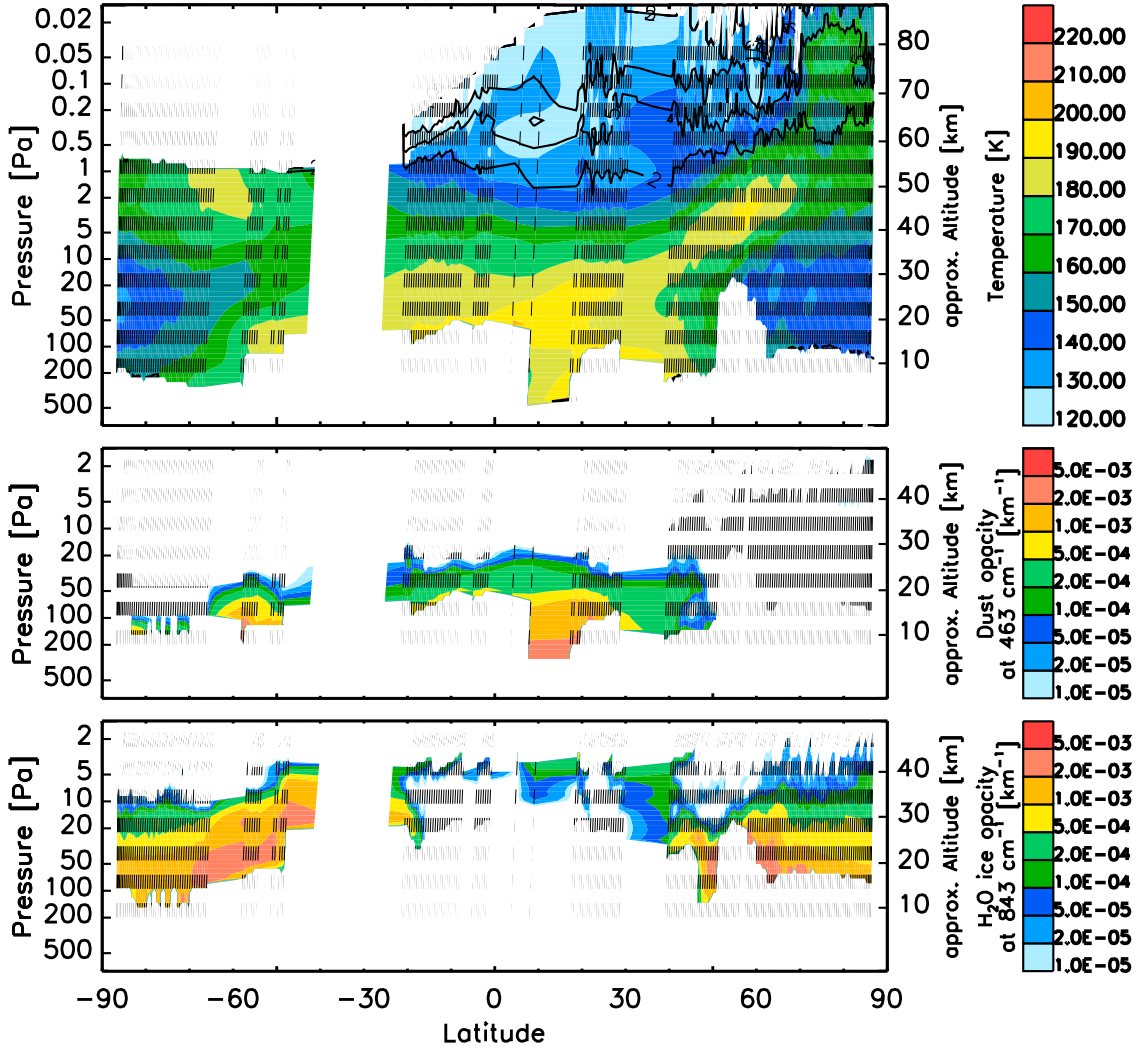
Figure 25. Retrieved profiles of (top) temperature and (middle) dust and (bottom) water ice opacity for different latitude bands in an L_s range from $111°$ to $120°$ at local times between 2100 and 0900 MLT. Individual profiles are shown in gray. The black solid line is the average of the individual profiles, with the black dashed lines giving the standard deviation. The black dotted line indicates the CO_2 frost point.

[126] Figure 25 shows retrieved profiles of temperature, dust, and water ice opacity for different latitude bands at the start of the mission. In the south polar region temperatures follow the CO_2 frost point remarkably closely at pressures above 10 Pa. In the altitude region of the middle atmospheric polar warming between 0.1 and 1 Pa the temperature rises to about 165 K at this season, and individual profiles show temperatures above 180 K. Little dust is observed where the temperature is significantly higher than the CO_2 frost point. There is evidence for the presence of water ice in the south polar region at this season although the opacity seems to be highly variable. Note that opacities in regions where the temperature is close to the CO_2 frost point are not reported as they may be contaminated by CO_2 ice. In the latitude range between $50°S$ and $40°S$ Figure 25 shows temperatures around 180 K in the lower atmosphere. Temperatures are generally decreasing with altitude, apart from a weak maximum at $1–2$ Pa. At pressures below ~ 0.5 Pa temperatures get very cold. Values below 140 K are common and values even below 120 K are reached. Although the average of these temperature profiles stays significantly above the CO_2 frost point, individual profiles get very close to it, indicating the potential for the formation of CO_2 ice clouds at these altitudes during this season. It is possible that some of the variability in the temperature profiles at these altitudes may actually be caused by opacity due to CO_2 ice, which is mistaken as opacity from gaseous CO_2 by the temperature retrieval. Very little dust is observed in this latitude band as it is close to the clear region shown in Figure 24. Water ice clouds can be present in this latitude band but their occurrence seems to be highly variable.

[127] Looking at measurements close to the equator in Figure 25, temperatures do not look very different from southern midlatitudes. However, between 1 and 2 Pa a weak temperature minimum is now found where individual temperature profiles get close to the CO_2 frost point. At equatorial latitudes dust seems to be present to higher altitudes and also seems to be less variable than elsewhere on the planet. The opacity level of 10^{-3} km^{-1} is located around 80 Pa while the 10^{-4} km^{-1} level is located around 30 Pa. Note that this falloff is significantly steeper than a homogeneously mixed profile, which would be represented by a diagonal line in the dust plots of Figure 25. High amounts of water ice are observed in the equatorial region as the time between $L_s = 111°$ and $120°$ corresponds to a season where the aphelion cloud is present [*M. D. Smith et al.*, 2001]. Water ice opacities up to $4 \cdot 10^{-3}$ km^{-1} are observed over a significant altitude range. As this is the maximum water ice opacity the MCS retrieval code is currently setup to retrieve, it is likely that water ice opacities actually exceed these levels.

[128] Toward the northern midlatitudes and the northern polar region temperature seems to get less variable and warmer in the middle and higher atmosphere. In the northern polar region temperature becomes essentially isothermal at a level of about 160 K at pressures below 20 Pa. Dust seems to decrease in average opacity and does not seem to reach as high altitudes as in the equatorial region. It is characterized by a high variability. Water ice seems to have a predominantly layered structure with peak opacities located around 50 Pa in both northern middle and northern polar latitudes. The maximum altitude at which ice is observed tends to decrease toward the pole.

Figure 26. As in Figure 24 but for an orbit on 16 February 2007 ($L_s = 185°$) during limb-staring measurements.
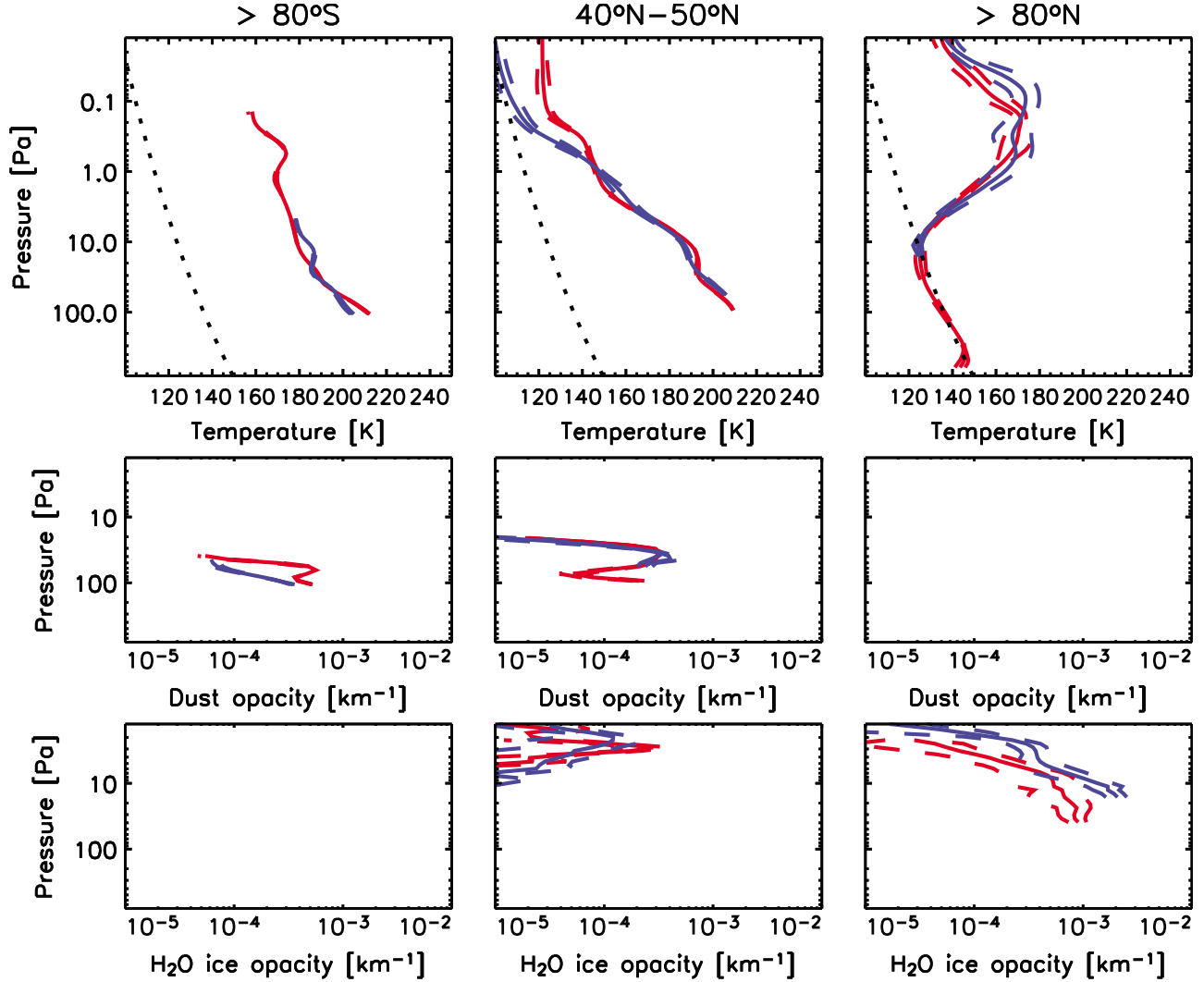
5.3. Limb-Staring Period, Northern Fall

[129] Because of difficulties with the instrument elevation actuator, MCS was operated in a mode termed limb staring most of the time between 9 February 2007 and 14 June 2007. During limb staring, MCS was pointed at the Mars limb at a constant elevation angle relative to the spacecraft, which resulted in reduced altitude coverage (<55 km) in the southern hemisphere. In the north polar region, coverage lifted off the limb, so that the lowest $1-2$ scale heights of the atmosphere could not be observed.

[130] Figure 26 shows a transect of nighttime measurements of an orbit on 16 February 2007, corresponding to an L_s of 185°. The individual measurements are closer to each other than during limb scanning because no calibration or on-planet measurements are taken between the limb measurements. Instrument stability allows interpolation of calibration parameters over times with no calibration measurements. However, the lack of calibration measurements reduces the accuracy of the data. This effect is worst for low radiances, like in a cold atmosphere at high altitudes, or for low amounts of dust or ice opacity. In southern middle and high latitudes the upper end of the MCS altitude coverage only reaches about 1 Pa (50–60 km). One can see that the temperature inversion is still present at this season, although the atmosphere has warmed up compared to $L_s = 111°$. Water ice is still present and the region between 50°S and 70°S, but the region now shows significant dust opacity not seen in the earlier season. In fact, the gap in retrievals between about 20°S and 50°S is caused by aerosol opacity which is too high for a successful retrieval.

[131] In the northern polar region the lower atmosphere has cooled down significantly compared to $L_s = 111°$. Water ice is present in this region but no significant dust opacity can be detected. It is likely that the dust in the north polar region is confined below 20 km at this season, so that MCS cannot detect to it because of the limb-staring geometry. In the higher atmosphere of the north polar region a strong temperature inversion is now observed. It is remarkable that the tongue of warm air reaches temperatures in excess of 190 K around 2 Pa, and extends into equatorial latitudes.

Figure 27. Averages of limb-staring measurements at $L_s = 248.1°$ (blue) in comparison with averages of limb-scanning measurements 1 day later around $L_s = 248.7°$ (red). Dashed lines give the standard deviations.

The presence of strong temperature inversions in both polar regions indicates a two-cell circulation at this season, in which downwelling occurs simultaneously over both poles.

[132] Although the MCS instrument was limb staring for most of the time between 9 February 2007 and 14 June 2007, for about one orbit on 31 May 2007 ($L_s = 248.7°$) it was put back into nominal limb-scanning mode for test purposes. For this period a regular calibration of the data could be performed. We use this period to get a better understanding of the data quality during limb staring.
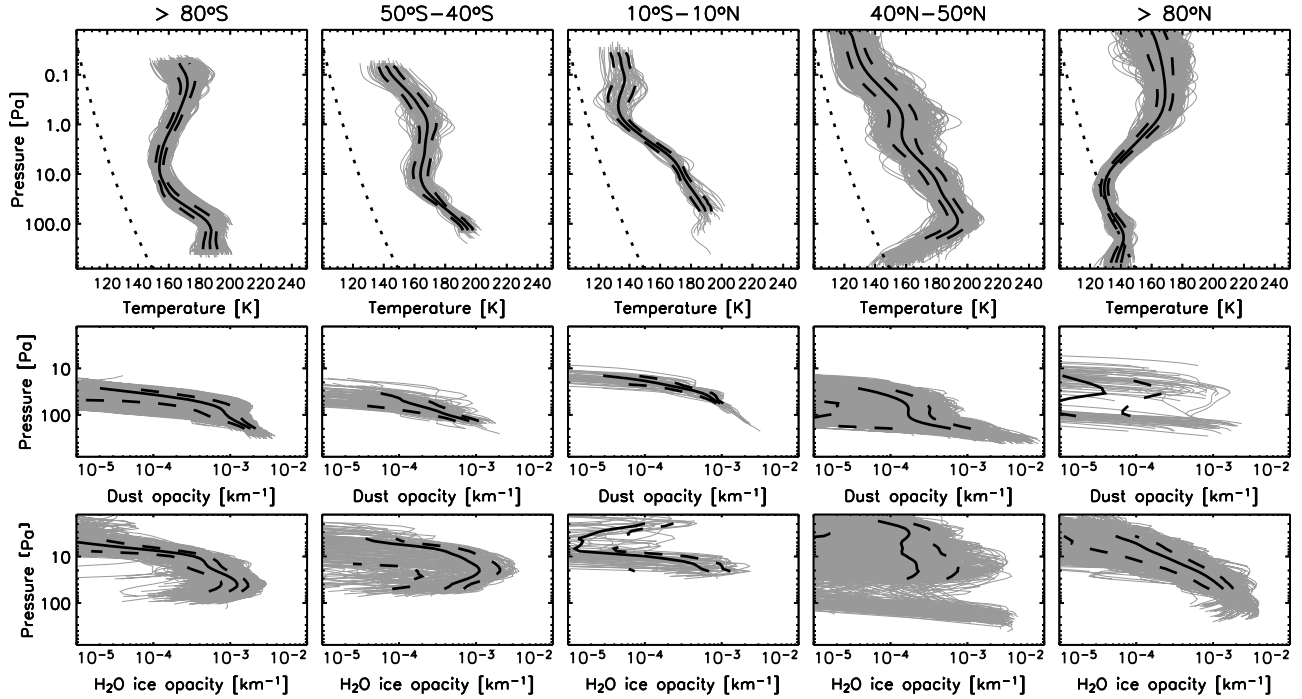
[133] Figure 27 shows averages of measurements obtained during this brief scanning period in latitude bands where data is available. They are compared with limb-staring measurements from an orbit on the day before ($L_s = 248.1°$), which covers similar latitudes and longitudes as the orbit during which limb scanning was performed. In Figure 27 (top) temperature comparisons are shown. One can easily see the limited coverage of the limb-staring profiles in the north and south polar regions. However, in the altitude range covered by the limb-staring profiles the agreement with the limb-scanning profiles is within the

standard deviations of the averages. In northern midlatitudes there are somewhat larger differences at high altitudes, which can be attributed to calibration uncertainties during the limb-staring period. These calibration uncertainties are most relevant when radiances are low, like in regions with low temperatures at high altitudes.

[134] For dust and water ice in Figure 27 the structure of the retrieved profiles is similar in limb-staring and limb-scanning measurements where retrievals are available. There are differences in the actual opacities on certain pressure levels. However, dust and water ice tend to be more variable in time and longitude than temperature, so this level of agreement can probably be considered as reasonable.

5.4. Limb-Scanning Period, Northern Winter/Spring

[135] After 14 June 2007, the MCS instrument was able to return to a limb-scanning mode, which included limb tracking and interspersed limb observations with space and occasional blackbody calibrations. Shortly after the return to limb scanning, a global dust storm broke out and

Figure 28. As in Figure 25 (2100–0900 MLT) but about half a Mars year later ($L_s = 330°–340°$), after the decay of the dust storm.

obscured the planet for several months. Although MCS was able to map the progress of the storm, limb measurements were difficult or impossible to retrieve because of the high dust loading. As the dust cleared, retrievals were possible over broader and broader geographic regions. Figure 28 shows temperature, dust, and water ice opacity profiles for selected latitude bands in the L_s range from 330° to 340° at which point successful retrievals occurred globally. In comparison to Figure 25 one notices that temperatures are higher throughout the atmosphere at nearly all latitudes. For example, temperatures at 10 Pa around the equator are around 175 K, compared to 160 K half a Mars year earlier. This is likely to be related to the dust loading, which is still higher than half a Mars year before. An opacity level of 10^{-3} km^{-1} is located around 60 Pa while the 10^{-4} km^{-1} level is located around 20 Pa. The falloff of the dust profiles seems to be significantly steeper than homogeneously mixed also in this season. Water ice is also present in the atmosphere at this season, in particular in both polar regions. Note that the lower atmosphere in the northern polar region has cooled down to the frost point of CO_2 and in the higher atmosphere the characteristic Martian polar winter temperature inversion is observed. At middle and low latitudes water ice is also present, mostly located above the dust layer, and its distribution is more variable than in the polar regions.

6. Comparison With MGS TES and Radio Science

[136] To validate the quality of the MCS temperature profiles, we have begun a comparison with previous observations. No comparable data sets exist for dust and ice profiles in published literature. However, work has been
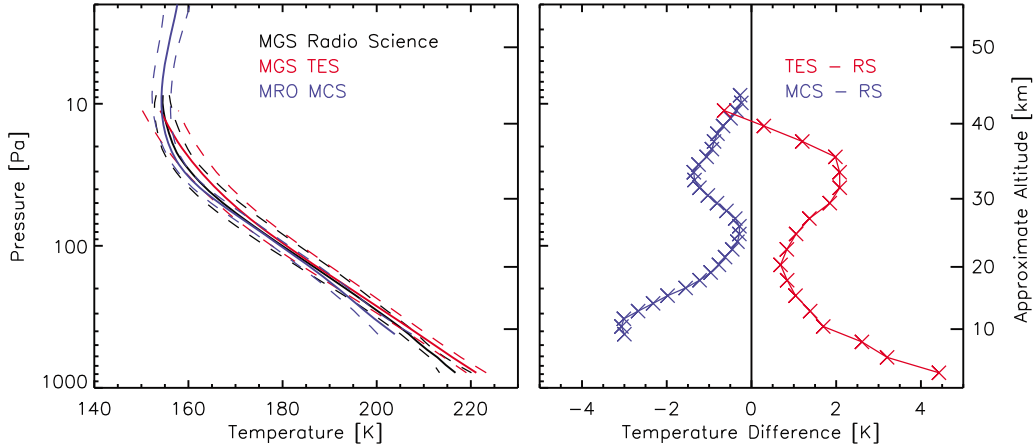
done on dust and ice limb profile retrievals from TES [*McConnochie and Smith*, 2008a, 2008b] that will make a comparison of these quantities possible in the future. Extensive sets of temperature profiles were obtained both by the TES instrument [*Conrath et al.*, 2000] and the radio science experiment [*Hinson et al.*, 1999], both on Mars Global Surveyor. TES profiles have about 10 km vertical resolution and are less influenced by aerosol than MCS limb measurements. Radio science measurements have about 1 km resolution and are not influenced by aerosol. Comparisons between these data sets were performed previously [*Hinson et al.*, 2004]. We chose to compare a subset of the data in a latitude range between 77°N and 82°N and an L_s range between 110° and 120°. We focus on this range because of the good coverage by both the MCS and the MGS radio science measurements. Furthermore the atmosphere does not show much year-to-year variability at this latitude and season [*Smith*, 2004]. A more detailed analysis covering a larger range of latitudes and seasons is beyond the scope of this paper but will be performed in the future.

[137] Table 5 summarizes the temperature profiles used in the comparison. Profiles from MCS, TES, and radio science

Table 5. Number and Time Ranges of Profiles for Averages Shown in Figure 29[a]

Measurement	Number of Profiles	Local Time Range (MLT)	L_s Range (deg)	Time of Acquisition
MRO MCS	424	0405–0450	111–120	Sep–Oct 2006
MGS TES	13,909	0305–0350	110–120	Jan–Feb 2001
MGS radio science	162	0255–0340	110–120	Jan–Feb 2001

[a]All measurements cover a latitude range between 77°N and 82°N.

Figure 29. (left) Averages of temperature profiles measured by MGS radio science (black), MGS TES (red), and MRO MCS (blue) as described in Table 5, with the dashed lines giving the standard deviation. (right) Differences between MGS radio science and MGS TES (red) and MRO MCS (blue). The crosses indicate the points on the TES and MCS pressure grids.

were averaged zonally on a common pressure grid for the given local time and L_s ranges.

[138] Figure 29 shows the result of the intercomparison. The three data sets agree very well with each other in capturing the decrease of temperature with altitude. Differences between MCS and radio science are generally below 2 K. This is particularly remarkable as the MCS measurements were taken in a different Mars year than the TES and radio science measurements. At low altitudes, MCS starts to deviate more strongly from the radio science measurements, which is likely related to the increased influence of aerosol. Differences between TES and radio science were investigated previously by *Hinson et al.* [2004] and are similarly small. TES does seem to overestimate temperatures slightly around 30 Pa. This is probably caused by the curvature in the temperature profile at these altitudes, which might not be captured in full detail by TES because of its coarser altitude resolution. Also MCS deviates more strongly from the radio science profile in this altitude region, although it seems to underestimate the temperatures. However, differences are within the standard deviations of the three sets of measurements, and the standard deviations themselves are of the same order of magnitude, suggesting that the variability in the temperatures is quite similar in the 2 Mars years studied.

7. Summary and Outlook

[139] This paper presents the radiative transfer and retrieval algorithm used to retrieve pressure as well as atmospheric profiles of temperature, dust and water ice opacity from Mars Climate Sounder limb measurements. The retrieval algorithm appears to perform well and does not introduce significant biases over most of the altitude range of the measurements. Measurements from the first Mars year of MCS observations have been retrieved and are being provided to the Planetary Data System.

[140] Retrieval results show several features of interest. Some examples include a strong warming over the winter pole, a pronounced minimum in water ice opacity in areas where these warm air masses reach lower altitudes, and

increasing dust opacities as the season progresses from northern summer to northern winter. Early intercomparisons with the historic data sets of MGS radio science and MGS TES temperatures show very good agreement with retrieved MCS temperatures. More comprehensive validation work is planned to cover a larger range of latitudes and seasons.

[141] Although this first version of MCS retrievals provides reasonable coverage of the planet, successful retrievals are still sparse in regions of high dust opacity and in the equatorial cloud belt. The use of additional channels in the dust and water ice retrieval will allow improved coverage in these regions. Adding a single scattering parameterization will improve the accuracy of the retrievals, in particular in conditions of higher dust or water ice opacities. The use of a scattering parameterization may also provide the opportunity to retrieve CO_2 ice.

[142] Another goal is to include nadir or off-nadir measurements into the limb profile retrieval where such measurements are available. This will give information on surface temperature and near-surface temperature, and thus improve the temperature profiles in the lowest scale height of the atmosphere. Furthermore, dust and water ice optical depths from nadir measurements will help constrain the dust and water ice profiles in the lowest scale height, and will also allow the extraction of information on water vapor from radiances in the B2 channel of MCS.

[143] Eventually we are planning to implement a two-dimensional radiative transfer parameterization into the retrieval code. The approach for this will be to prescribe a horizontal gradient in the line-of-sight radiative transfer when performing a single profile retrieval. Because of the use of channels with significant opacities, pressure, and to some extent temperature retrievals can be influenced by a horizontally inhomogeneous atmosphere, as it exists for example close to the edge of the polar vortex. Accounting for these horizontal gradients should improve the accuracy of the pressure and temperature retrievals.

References

Brown, L. R., C. R. Humphrey, and R. R. Gamache (2007), CO_2-broadened water in the pure rotation and ν_2 fundamental regions, *J. Mol. Spectrosc.*, *246*, 1–21.

Burch, D. E., D. A. Gryvnak, R. R. Patty, and C. E. Bartky (1969), Absorption of infrared radiant energy by CO_2 and H_2O. IV. Shapes of collision-broadened CO_2 lines, *J. Opt. Soc. Am.*, *59*, 267–280.

Chahine, M. T. (1970), Inverse problems in radiative transfer: Determination of atmospheric parameters, *J. Atmos. Sci.*, *27*, 960–967.

Chahine, M. T. (1972), A general relaxation method for inverse solution of the full radiative transfer equation, *J. Atmos. Sci.*, *29*, 741–747.

Clancy, R. T., M. J. Wolff, and P. R. Christensen (2003), Mars aerosol studies with the MGS TES emission phase function observations: Optical depths, particle sizes, and ice cloud types versus latitude and solar longitude, *J. Geophys. Res.*, *108*(E9), 5098, doi:10.1029/2003JE002058.

Clancy, R. T., M. J. Wolff, B. A. Whitney, B. A. Cantor, and M. D. Smith (2007), Mars equatorial mesospheric clouds: Global occurrence and physical properties from Mars Global Surveyor Thermal Emission Spectrometer and Mars Orbiter Camera limb observations, *J. Geophys. Res.*, *112*, E04004, doi:10.1029/2006JE002805.

Conrath, B. J. (1975), Thermal structure of the Martian atmosphere during the dissipation of the dust storm of 1971, *Icarus*, *24*, 36–46.

Conrath, B. J., J. C. Pearl, M. D. Smith, W. C. Maguire, P. R. Christensen, S. Dason, and M. S. Kaelberer (2000), Mars Global Surveyor Thermal Emission Spectrometer (TES) observations: Atmospheric temperatures during aerobraking and science phasing, *J. Geophys. Res.*, *105*, 9509–9519.

Curtis, A. R. (1952), Discussion of a statistical model for water vapour absorption, *Q. J. R. Meteorol. Soc.*, *78*, 638–640.

Fedorova, A. A., O. I. Korablev, J.-L. Bertaux, A. V. Rodin, F. Montmessin, D. A. Belyaev, and A. Reberac (2009), Solar infrared occultation observations by SPICAM experiment on Mars-Express: Simultaneous measurements of the vertical distributions of H_2O, CO_2 and aerosol, *Icarus*, *200*, 96–117.

Godson, W. L. (1953), The evaluation of infrared-radiative fluxes due to atmospheric water vapour, *Q. J. R. Meteorol. Soc.*, *79*, 367–379.

Hansen, G. B. (1997), The infrared absorption spectrum of carbon dioxide ice from 1.8 to 333 μm, *J. Geophys. Res.*, *102*, 21,569–21,587.

Hansen, G. B. (2003), Infrared optical constants of Martian dust derived from Martian spectra, in *Sixth International Conference on Mars, July 20–25, 2003, Pasadena, CA* [CD-ROM], *LPI Contrib.*, *1164*, Abstract 3194.

Hinson, D. P., R. A. Simpson, J. D. Twicken, G. L. Tyler, and F. M. Flasar (1999), Initial results from radio occultation measurements with Mars Global Surveyor, *J. Geophys. Res.*, *104*, 26,997–27,012.

Hinson, D. P., M. D. Smith, and B. J. Conrath (2004), Comparison of atmospheric temperatures obtained through infrared sounding and radio occultation by Mars Global Surveyor, *J. Geophys. Res.*, *109*, E12002, doi:10.1029/2004JE002344.

Irwin, P. G. J. (2007), Limb scattering calculations, *Tech. Rep. MCS/OX/TR/ 63*, Univ. of Oxford, Oxford, U. K.

Krasnopolsky, V. A., G. L. Bjoraker, M. J. Mumma, and D. E. Jennings (1997), High-resolution spectroscopy of Mars at 3.7 and 8 μm: A sensitive search for H_2O_2, H_2CO, HCl, and CH_4, and detection of HDO, *J. Geophys. Res.*, *102*, 6525–6534.

Lopez-Valverde, M. A., and M. Lopez-Puertas (1994a), A non-local thermodynamic equilibrium radiative transfer model for infrared emissions in the atmosphere of Mars: 1. Theoretical basis and nighttime populations of vibrational levels, *J. Geophys. Res.*, *99*, 13,093–13,115.

Lopez-Valverde, M. A., and M. Lopez-Puertas (1994b), A non-local thermodynamic equilibrium radiative transfer model for infrared emissions in the atmosphere of Mars: 2. Daytime populations of vibrational levels, *J. Geophys. Res.*, *99*, 13,117–13,132.

McCleese, D. J., R. D. Haskins, J. T. Schofield, R. W. Zurek, C. B. Leovy, D. A. Paige, and F. W. Taylor (1992), Atmosphere and climate studies of Mars using the Mars Observer pressure modulator infrared radiometer, *J. Geophys. Res.*, *97*, 7735–7757.

McCleese, D. J., J. T. Schofield, F. W. Taylor, S. B. Calcutt, M. C. Foote, D. M. Kass, C. B. Leovy, D. A. Paige, P. L. Read, and R. W. Zurek (2007), Mars Climate Sounder: An investigation of thermal and water vapor structure, dust and condensate distributions in the atmosphere, and energy balance of the polar regions, *J. Geophys. Res.*, *112*, E05S06, doi:10.1029/2006JE002790.

McCleese, D. J., et al. (2008), Intense polar warming of the middle atmosphere on Mars, *Nat. Geosci.*, *1*, 745–749.

McConnochie, T. H., and M. D. Smith (2008a), Vertically resolved water ice aerosols opacity from Mars Global Surveyor Thermal Emission Spectrometer (TES) limb sounding, paper presented at Mars Water Cycle Workshop, Serv. d'Aeron., Paris.

McConnochie, T. H., and M. D. Smith (2008b), Vertically resolved aerosol climatology from Mars Global Surveyor Thermal Emission Spectrometer (MGS-TES) limb sounding, paper presented at Third International Workshop on the Mars Atmosphere, Lunar and Planet. Inst., Williamsburg, Va.

Montmessin, F., E. Quémerais, J. L. Bertaux, O. Korablev, P. Rannou, and S. Lebonnois (2006), Stellar occultations at UV vavelengths by the SPICAM instrument: Retrieval and analysis of Martian haze profiles, *J. Geophys. Res.*, *111*, E09S09, doi:10.1029/2005JE002662.

Montmessin, F., B. Gondet, J.-P. Bibring, Y. Langevin, P. Drossart, F. Forget, and T. Fouchet (2007), Hyperspectral imaging of convective CO_2 ice clouds in the equatorial mesosphere of Mars, *J. Geophys. Res.*, *112*, E11S90, doi:10.1029/2007JE002944.

Owen, T., K. Biemann, D. R. Rushneck, J. E. Biller, D. W. Howarth, and A. L. Lafleur (1977), The composition of the atmosphere at the surface of Mars, *J. Geophys. Res.*, *82*, 4635–4639.

Richardson, M. I., A. D. Toigo, and C. E. Newman (2007), PlanetWRF: A general purpose, local to global numerical model for planetary atmospheric and climate dynamics, *J. Geophys. Res.*, *112*, E09001, doi:10.1029/2006JE002825.

Rothman, L. S., et al. (2005), The HITRAN 2004 molecular spectroscopic data base, *J. Quant. Spectrosc. Radiat. Transfer*, *96*, 139–204.

Smith, D. E., et al. (2001), Mars Orbiter Laser Altimeter: Experiment summary after the first year of global mapping of Mars, *J. Geophys. Res.*, *106*, 23,689–23,722.

Smith, M. D. (2004), Interannual variability in TES atmospheric observations of Mars during 1999–2003, *Icarus*, *167*, 148–165.

Smith, M. D., J. C. Pearl, B. J. Conrath, and P. R. Christensen (2001), Thermal Emission Spectrometer results: Mars atmospheric thermal structure and aerosol distribution, *J. Geophys. Res.*, *106*, 23,929–23,946.

Tillman, J. E., N. C. Johnson, P. Guttorp, and D. B. Percival (1993), The Martian annual atmospheric pressure cycle: Years without great dust storms, *J. Geophys. Res.*, *98*, 10,963–10,971.

Warren, S. G. (1984), Optical constants of ice from the ultraviolet to the microwave, *Appl. Opt.*, *23*, 1206–1225.

Whitney, B. A., M. J. Wolff, and R. T. Clancy (1999), Monte Carlo radiation transfer models for Mars, in *Fifth International Conference on Mars, July 18–23, 1999, Pasadena, CA* [CD-ROM], *LPI Contrib.*, *972*, Abstract 6213.

Wolff, M. J., and R. T. Clancy (2003), Constraints on the size of Martian aerosols from Thermal Emission Spectrometer observations, *J. Geophys. Res.*, *108*(E9), 5097, doi:10.1029/2003JE002057.

Wolff, M. J., et al. (2006), Constraints on dust aerosols from the Mars Exploration Rovers using MGS overflights and Mini-TES, *J. Geophys. Res.*, *111*, E12S17, doi:10.1029/2006JE002786.

Yamamoto, G., M. Tanaka, and T. Aoki (1969), Estimation of rotational line widths of carbon dioxide bands, *J. Quant. Spectrosc. Radiat. Transfer*, *9*, 371–382.

Zuber, M. T., et al. (1998), Observations of the north polar region of Mars from the Mars Orbiter Laser Altimeter, *Science*, *282*, 2053–2060.

Zurek, R. W., and S. E. Smrekar (2007), An overview of the Mars Reconnaissance Orbiter (MRO) science mission, *J. Geophys. Res.*, *112*, E05S01, doi:10.1029/2006JE002701.

———————————

W. A. Abdou, C. R. Backus, D. M. Kass, A. Kleinböhl, D. J. McCleese, J. T. Schofield, B. Sen, and J. H. Shirley, Jet Propulsion Laboratory, California Institute of Technology, Mail Stop 169-237, 4800 Oak Grove Drive, Pasadena, CA 91109, USA. (armin.kleinboehl@jpl.nasa.gov)

W. G. Lawson and M. I. Richardson, Division of Geological and Planetary Sciences, California Institute of Technology, Mail Code 170-25, 1200 East California Boulevard, Pasadena, CA 91125, USA.

F. W. Taylor and N. A. Teanby, Clarendon Laboratory, Atmospheric, Oceanic, and Planetary Physics, University of Oxford, Parks Road, Oxford OX1 3PU, UK.